Automatic extraction of *Sargassum* features from Sentinel-2 MSI images

Mengqiu Wang and Chuanmin Hu*

***Abstract*— Frequent *Sargassum* beaching in the Caribbean Sea and other regions has caused severe problems for local environments and economies. Although coarse-resolution satellite instruments can provide large-scale *Sargassum* distributions, their use is limited in nearshore waters that are directly relevant to local communities. Finer-resolution instruments, such as the Multispectral instruments (MSI) on the Sentinel-2 satellites, show potential to fill this gap, yet automatic *Sargassum* extraction is problematic due to compounding factors. In this paper, a new approach is developed to extract *Sargassum* features automatically from MSI Floating Algae Index (FAI) images. Because of the high spatial resolution, limited Signal to Noise Ratio (SNR), and staggered instrument internal configuration, there are many non-algae bright targets (including cloud artifacts and wave-induced glints) causing enhanced near-infrared reflectance and elevated FAI values. Based on the spatial patterns of these image "noises", a Trainable Nonlinear Reaction Diffusion (TNRD) denoising model is trained to estimate and remove such noise. The model shows excellent performance when tested over realistic noise patterns derived from MSI measurements. After removing such noise and masking clouds (as well as cloud shadows and glint patterns), biomass density from each valid pixel is quantified using the FAI-biomass model established from earlier field measurements, from which *Sargassum* morphology (length/width/biomass) is derived. Overall, the proposed approach achieves over 86% *Sargassum* extraction accuracy and shows preliminary success on Landsat-8 images. The approach is expected to be incorporated in the existing near real-time *Sargassum* Watch System for both Landsat-8 and Sentinel-2 observations to monitor *Sargassum* over nearshore waters.**

***Index Terms*— Multispectral instruments (MSI), Operational Land Imager (OLI), Floating Algae Index (FAI), *Sargassum*, feature extraction, denoising**

I. Introduction

SINCE 2011, recurrent *Sargassum* blooms and severe beaching events have been impacting the Caribbean Sea (CS) and tropical Atlantic regions [1-9]. Despite their important ecological benefits in the open ocean [10-12], massive influx of pelagic *Sargassum* accumulated on beaches can negatively affect the local tourism, economy, environment, and coastal ecosystem [13-17]. Decayed *Sargassum* deteriorate water quality via consuming oxygen and releasing hydrogen sulfide and organic decomposition products [19-20], leading to seagrass and coral reef mortality during major bloom events [20]. Several studies have suggested that large-scale wind and circulation patterns (e.g., the North Atlantic Oscillation or NAO, Inter-Tropical Convergence Zone or ITCZ, deep-water mixing) as well as increased anthropogenic nutrient supply may have caused the recent *Sargassum*

blooms and could support future bloom development if the situation continues [7, 21-24].

Timely reporting of *Sargassum* locations and amounts can help planning with research and mitigation actions (e.g., physical removal of *Sargassum* at sea and on the beach). In previous efforts, most information has been provided through satellite remote sensing. Of the various satellite sensors used for this purpose, large-swath but coarse-resolution sensors such as the Moderate Resolution Imaging Spectroradiometer (MODIS), Visible Infrared Imaging Radiometer Suite (VIIRS), MEdium Resolution Imaging Spectrometer (MERIS), and Ocean Land Colour Instrument (OLCI) can be used to derive *Sargassum* distribution maps at synoptic scale [1,3,5,7-8]. In these applications, several indexes such as the Maximum Chlorophyll Index (MCI) [25], Floating Algae Index (FAI) [26] or Alternative FAI (AFAI) [3] have been used to detect *Sargassum* presence and quantify *Sargassum* abundance. In particular, an operational *Sargassum* Watch System (SaWS, [15]) has been implemented to use MODIS and VIIRS data to provide *Sargassum* distributions in several regions of the Atlantic Ocean (including the Gulf of Mexico (GOM) and CS).

However, several limitations exist with these coarse-resolution imagery (~1-km or lower resolution). First, they cannot be used to detect small *Sargassum* features. For example, the lower detection limit of MODIS was estimated to be 0.2% of a 1-km pixel [3], equivalent to about 2 m × 1 km in *Sargassum* size. Second, the coarse-resolution pixels are treated as clouds even with partial cloud cover, resulting in higher cloud coverage and fewer valid observations when compared with higher-resolution imagery [27]. Lastly, because of the interference of shallow-water bottom and/or high concentrations of total suspended particles, as well as the presence of mixed pixels containing land and water, there are often no valid *Sargassum* observations in nearshore waters [3]. For this reason, in SaWS MODIS / VIIRS imagery, in order to avoid delivering false information in nearshore waters, these water pixels are masked up to 30 km offshore.

The higher-resolution multispectral imagery, on the other hand, are capable of avoiding these problems. In fact, the 30-m resolution Landsat FAI images have already been used to study *Sargassum* distributions in the northern GOM [15, 28], and to guide short-term predictions in the *Sargassum* Early Advisory System (SEAS) where human inspection is involved to interpret the *Sargassum* features in the Landsat images [29]. Similar to the Landsat multispectral sensors, the Multi-spectral instruments (MSI) carried on the two European Space Agency's (ESA) Sentinel-2 (S2) satellites (Sentinel-2A (S2A, 23-Jun 2015) and 2B (S2B, 7-Mar 2017)) are also equipped with the spectral bands to detect floating vegetation signals. These S2 MSI images provide valuable measurements over the entire CS and GOM where the *Sargassum* blooms frequently occur [30]. With two satellites combined, the MSI images (with 10/20-m resolution) can achieve 5-day revisits, therefore having great potentials for *Sargassum* monitoring over coastal and nearshore waters. Fig.1 shows an example of the MSI FAI image where various *Sargassum* features can be visualized.

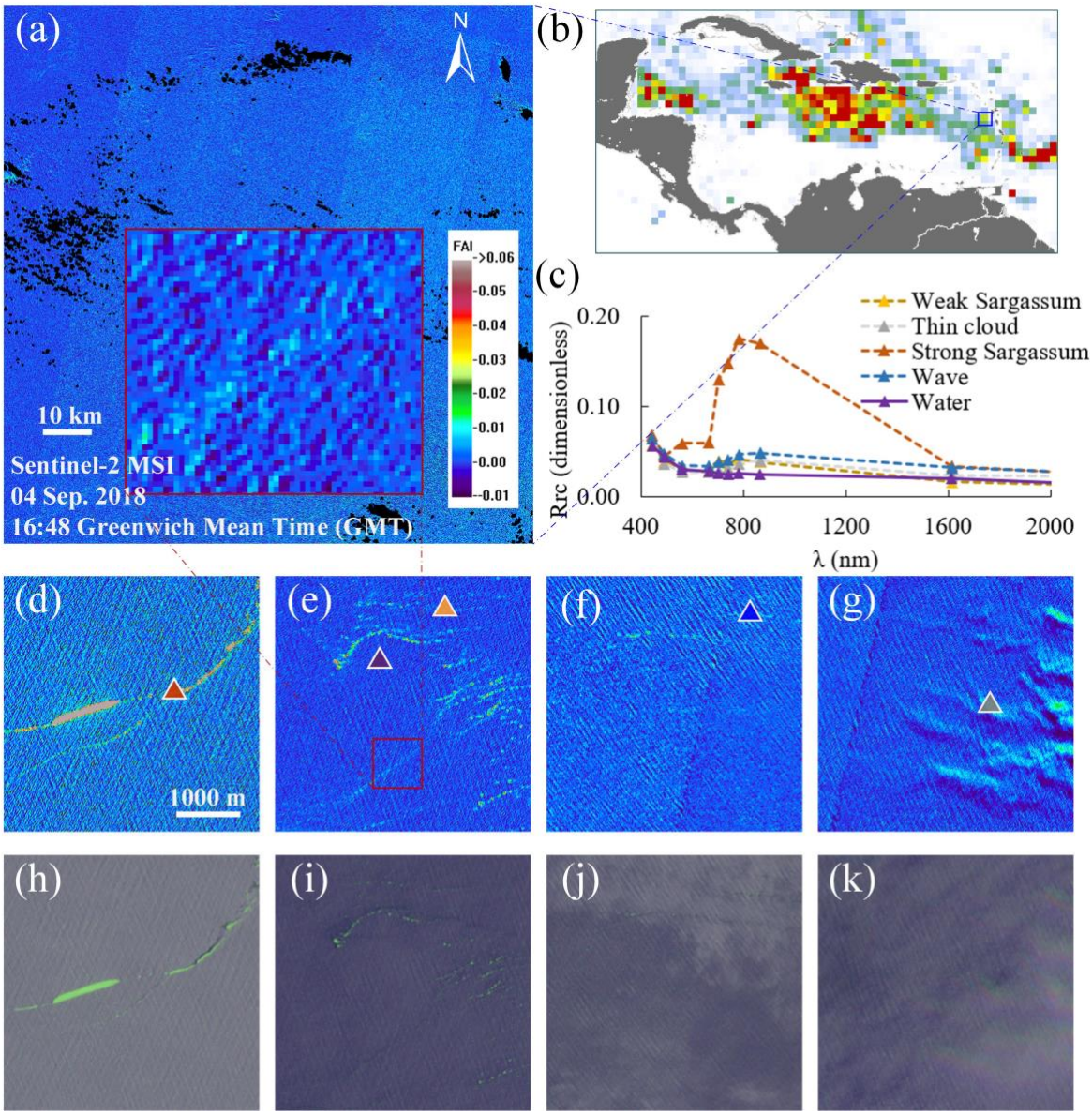

Fig. 1. (a) Sentinel-2 MSI FAI image (T20PNC) acquired on September 4th, 2018, where its location is shown in the MODIS monthly mean *Sargassum* areal coverage map for September 2018 (b). (c) The reflectance spectra of the selected strong *Sargassum* (d), weak *Sargassum* (e), wave (f), thin cloud (g), and water pixels (colored triangles). Note that the observed "strong *Sargassum*" spectrum is different than those from other floating materials/algae reported by Biermann et al. (2020) and Qi et al. (2020) [31, 32]. (d-g) Examples of these features in the MSI FAI images, and (h-k) the corresponding false color Red-Green-Blue (RGB) images where band 4 (665 nm), the NIR band (865 nm), and band 2 (497 nm) are used as the red, green, and blue channels in the RGB images. The red box in (e) is enlarged to show that the weak *Sargassum* features can be very hard to delineate from the background water. The stripe noises can be visualized in (a), (f) and (g) (marked by red arrows). Note that the reflectance spectra of wave, thin cloud, and weak *Sargassum* features are all similar to each other.

Although *Sargassum* features in MSI FAI images can be identified by trained human analysts, because these features appear as bright, often elongated targets over background water, it is nearly impossible to apply the manual delineation method in an operational fashion in SaWS. This is because manual delineation is not only time consuming but also non-objective, especially considering that most of these *Sargassum* features are only a few pixels in size (Fig. 1). Therefore, automatic *Sargassum* extraction from the high-resolution MSI images is desired for practical applications in *Sargassum* monitoring and tracking. Thus, the objective of this paper is to develop a reliable and fully automatic method to extract *Sargassum* features from MSI images.

II. Data and Methods

A. Background of Sargassum feature extraction

On coarse-resolution satellite images such as those from MODIS or VIIRS, automatic extraction of *Sargassum* features or other macroalgae features is typically realized through threshold-based segmentation, where the key steps are to reduce false-positive detection (such as from clouds and noises) and to reconstruct the background variations [3, 33-35]. In this study, following previous works (refs), we use MSI FAI images to extract *Sargassum* features. The selection of FAI over MCI-like index (note that MSI is equipped with a 704-nm band, thus possible to calculate MCI value for each pixel (Gower et al.)) is to 1) assure consistency with earlier studies using either FAI or alternative FAI (refs) and 2) avoid interference of water-column algal blooms as these blooms also show high MCI values (Gower et al….). On finer-resolution MSI FAI images, automatic extraction of *Sargassum* pixels suffers from confusing bright targets caused by clouds, sun glint and sky glint reflection of the surface waves (Fig. 1), etc. These waves induce spatially coherent patterns on the FAI images (Figs. 1d-g), where the wave-induced features can even be stronger than the weak *Sargassum* signals. Similarly, cloud pixels also show enhanced reflectance in the NIR (and therefore high FAI values) comparing to the nearby water pixels (Fig. 1g). In addition, because different MSI bands are not sampled simultaneously due to its special instrument design [36], for faster moving clouds, some pixels may have their red-band signals from water but NIR-band signals from clouds. Consequently, even thin clouds can show strong positive FAI values (Fig. 1g). For the same reason, the FAI signals of surface wave patterns may also be intensified during wave propagation. All these confusing factors need to be accounted for when automatic extraction of *Sargassum* features is undertaken.

In the past, traditional methods such as Gaussian smoothing have been used to denoise VIIRS images [5]. However, the noise patterns on the MSI images are highly variable, and traditional methods will inevitably cause feature attenuation even after local adjustments for optimal performance. In addition to noise reduction, another major challenge in the automatic extraction of *Sargassum* features from MSI images, is the relatively large-scale variations in the image background, which can be due to both image stripe patterns [36] and changes in water's optical properties.

To account for these confounding factors, automatic extraction needs to remove clouds and other confusing features objectively. Below we describe the method in detail. Specifically, the Trainable Nonlinear Reaction Diffusion (TNRD) denoising model [37] is adopted here to minimize noise in the MSI FAI images, following which *Sargassum* features are extracted with feature biomass and morphology quantified. Finally, the applicability of this method to other similar high-resolution sensors is evaluated over Landsat-8 Operational Land Imager (OLI) data.

B. Data and preprocessing

In this study, 68 S2 L1C images collected near the Lesser Antilles Islands (tile: T20PNC and T20PQB) in 2018, containing less than 70% cloud coverage, were downloaded from the USGS earth explorer https://earthexplorer.usgs.gov/, and processed with ACOLITE software ([38], version 20190326) to generate Rayleigh-corrected reflectance (Rrc, unitless) at 10-m resolution. We recognize that different approaches have been used for aerosol correction [39], but because Rrc is not corrected for aerosol effects, these difference approaches would produce the same results in Rrc. The Rrc data in the RED, Near-Infrared (NIR), and ShortWave-Infrared (SWIR) bands were used to calculate FAI for each pixel [26]:

$$FAI = Rrc_{NIR} - Rrc'_{NIR}$$

$$Rrc'_{NIR} = Rrc_{RED} + (Rrc_{SWIR} - Rrc_{RED}) \times (\lambda_{NIR} - \lambda_{RED}) / (\lambda_{SWIR} - \lambda_{RED}) \quad (1)$$

where λ_{RED} = 665 nm (band 4), λ_{NIR} = 865 nm (band 8A), λ_{SWIR} = 1610 nm (band 11). The pixels with large Rrc_{1610} (> 0.10) were pre-masked to exclude land and bright cloud pixels. Similar to MSI, 5 Landsat-8 OLI images collected in the GOM and CS were also processed using the same ACOLITE software to generate Rrc data at 30-m resolution, from which FAI for each pixel was calculated using equation (1) with three Rrc bands centered at 655 nm, 865 nm, and 1609 nm, respectively.

To compare the observation capacities between different sensors, MODIS Aqua and Terra Level-0 data collected in the Central West Atlantic in 2018 were downloaded from the U.S. National Aeronautics and Space Administration (NASA) Goddard Space Flight Center (http://oceancolor.gsfc.nasa.gov), and processed to general Rrc data using the SeaDAS software (version 7.5). The corresponding MODIS AFAI images were generated using Rrc data in the spectral bands centered at 667nm, 748nm, and 869nm (Eq. 1). The *Sargassum*-containing pixels were extracted using the method described in Wang and Hu (2016), whose biomass densities were estimated using the AFAI-biomass model described in Wang et al. (2018). These data are used to compare with the simultaneous and co-located MSI observations.

C. Technical Approach

As shown in Fig. 2, the workflow for *Sargassum* extraction and quantification consists of four major components: 1) Masking clouds and other non-*Sargassum* bright targets, based on the local high reflectance in the SWIR bands; 2) TNRD-based denoising to reduce false positive features on the FAI images; 3) Background estimation and *Sargassum* extraction from the pre-processed FAI images to delineate the *Sargassum*-containing pixels; 4) Quantification of the *Sargassum* biomass density for the *Sargassum*-containing pixels.

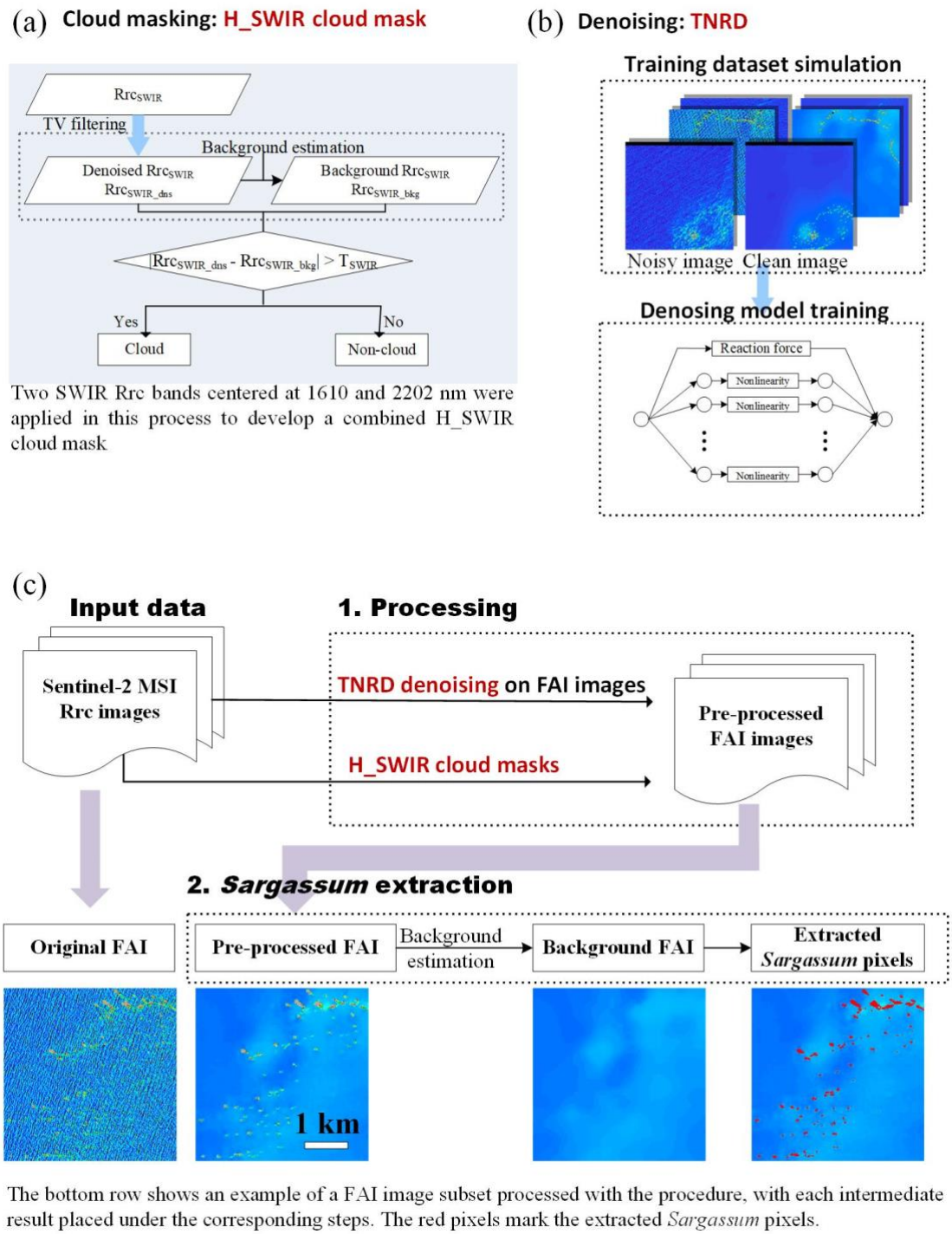

Fig. 2. The workflow to extract *Sargassum*-containing pixels from S2 MSI images while masking other unwanted features. The cloud masking and the TNRD model training processes are described in (a) and (b), respectively. These two processes are included in the first step of image processing in (c), which shows the entire *Sargassum* extraction workflow. Results from a representative FAI image are inserted in (c) to demonstrate the individual steps in the classification process. The extracted *Sargassum* pixels are marked in red, from which a FAI-biomass density model is applied to estimate biomass density for each *Sargassum*-containing pixel.

1) Cloud masking

Similar to *Sargassum*, clouds often show higher FAI values than adjacent water pixels. To reduce these false-positive detections, cloud masking was conducted before extracting *Sargassum* features. On high-resolution images such as those from Landsat-8 OLI

and S2 MSI, the Function of mask (Fmask [40], https://github.com/GERSL/Fmask) algorithms have proven to have superior performance over many other approaches [41]. Because each MSI spectral band measures the ocean surface at slightly different time and under slightly different viewing geometry, for non-stationary objects with unknown altitude such as clouds, there is an observable parallax effect between spectral bands that is hard to correct [36]. Recently, Fmask (version 4.0) has integrated a cloud displacement index (CDI, [42]) to enhance the cloud detection performance. However, as shown in Fig. 3c, the improved Fmask still misses some small clouds with high FAI values, and can also over-mask the water pixels in regions under strong sun glint (Fig. 3g).

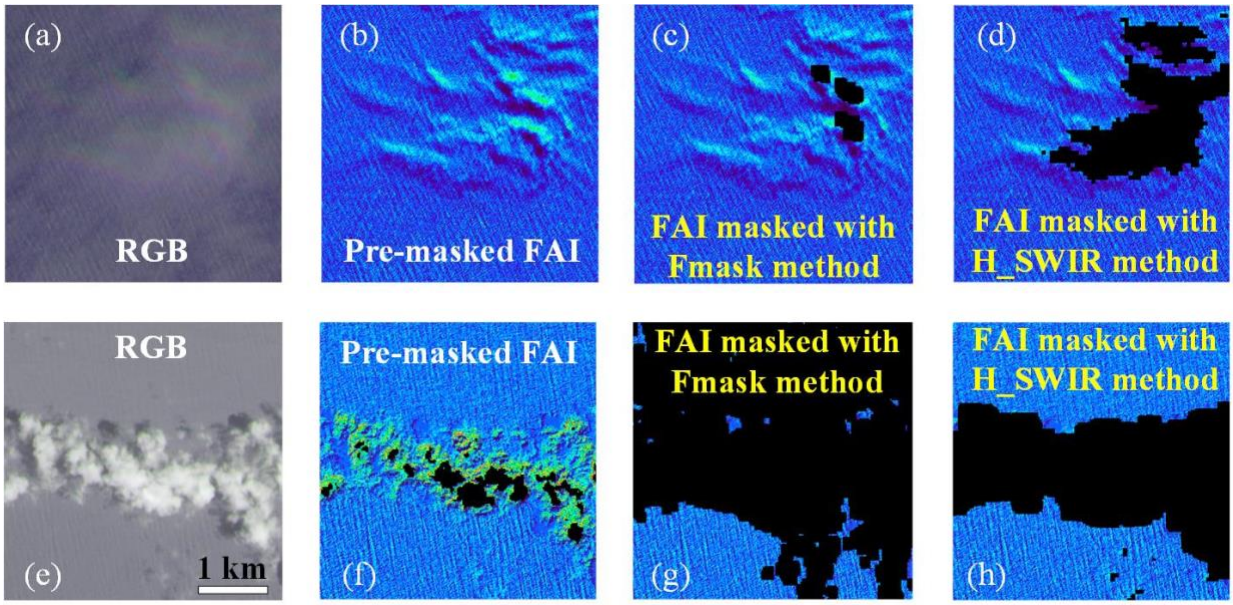

Fig. 3. Comparison of the cloud masking performance from the H_SWIR method (this study) and Fmask method (published approach) for two cases (top and bottom rows) on September 4th, 2018 in T20PNC. (a) and (e): RGB images; (b) and (f): FAI images pre-masked with the Rrc_{1610} threshold (some of the cloud pixels are masked in black in (f)); (c) and (g): FAI images masked with Fmask (published approach); (d) and (h): FAI images masked with the H_SWIR mask (this study). The black color represents the masked cloud pixels. The comparisons show that Fmask can over-mask in regions under strong sun glint (g) and under-mask in region under thin clouds (c).

Because of the relatively lower spatial variability of the water reflectance and less confusing bright surface structures, cloud detection on ocean images is actually less challenging than on land images. On moderate resolution images, many cloud masking methods utilize threshold-based segmentation from selected bands [3, 34, 43]. Here, a similar approach was developed to identify pixels with high reflectance in MSI bands 11 and 12 (1610 nm and 2202 nm). These two bands were selected because: 1) the temporal offsets between band 12 (2202nm) and band 8A (865 nm) and between band 11 (1610 nm) and band 6 (740 nm) are both small (0.030/0.057 seconds, https://earth.esa.int/web/sentinel/technical-guides/sentinel-2-msi/msi-instrument); 2) *Sargassum* features have lower reflectance than clouds in these SWIR bands.

Because there are many "noise" patterns from the wave-induced glint pixels, a total variance (TV) filtering (weight = 0.05) was first applied to Rrc images in both MSI bands 11 and 12 [44]. Cloud detection was then conducted on the denoised Rrc images. To

capture the large-scale image variations (as shown in Fig. 1a), the background ocean reflectance in bands 11 and 12 were estimated using an iterative mean background filtering with a 200 × 200 window size (the details of the background estimation method are described in the corresponding section below). Then, the pixels with local high reflectance can be extracted after subtracting the background with the corresponding segmentation threshold. Here, the cloud masking method is named as the H_SWIR method:

$$Rrc_{1610_{dns}} - Rrc_{1610_{bkg}} > T_{1610}, \&$$
$$Rrc_{2202_{dns}} - Rrc_{2202_{bkg}} > T_{2202} \quad (2)$$

where $Rrc_{1610_{dns}}$ is the denoised Rrc_{1610}, and $Rrc_{2202_{dns}}$ is the denoised Rrc_{2202}. $Rrc_{1610_{bkg}}$ is the estimated background Rrc_{1610}, and $Rrc_{2202_{bkg}}$ is the estimated background Rrc_{2202}.

Normalized and cumulative histograms of the representative *Sargassum*, water, and cloud pixels were used to determine the optimal thresholds (T_{1610} and T_{2202}) to minimize the effect of falsely detecting *Sargassum* and water pixels as clouds, resulting in T_{1610} = 0.010 and T_{2202} = 0.008 (Fig. 4). The threshold difference could be partly due to the sensitivity difference of the corresponding spectral bands used for cloud masking [45]. Such masked pixels were then dilated outward with a 20 × 20 window to mask the adjacent pixels. Fig. 3 suggests that the proposed H_SWIR cloud masking method has improved performance over the published Fmask method on MSI FAI images.

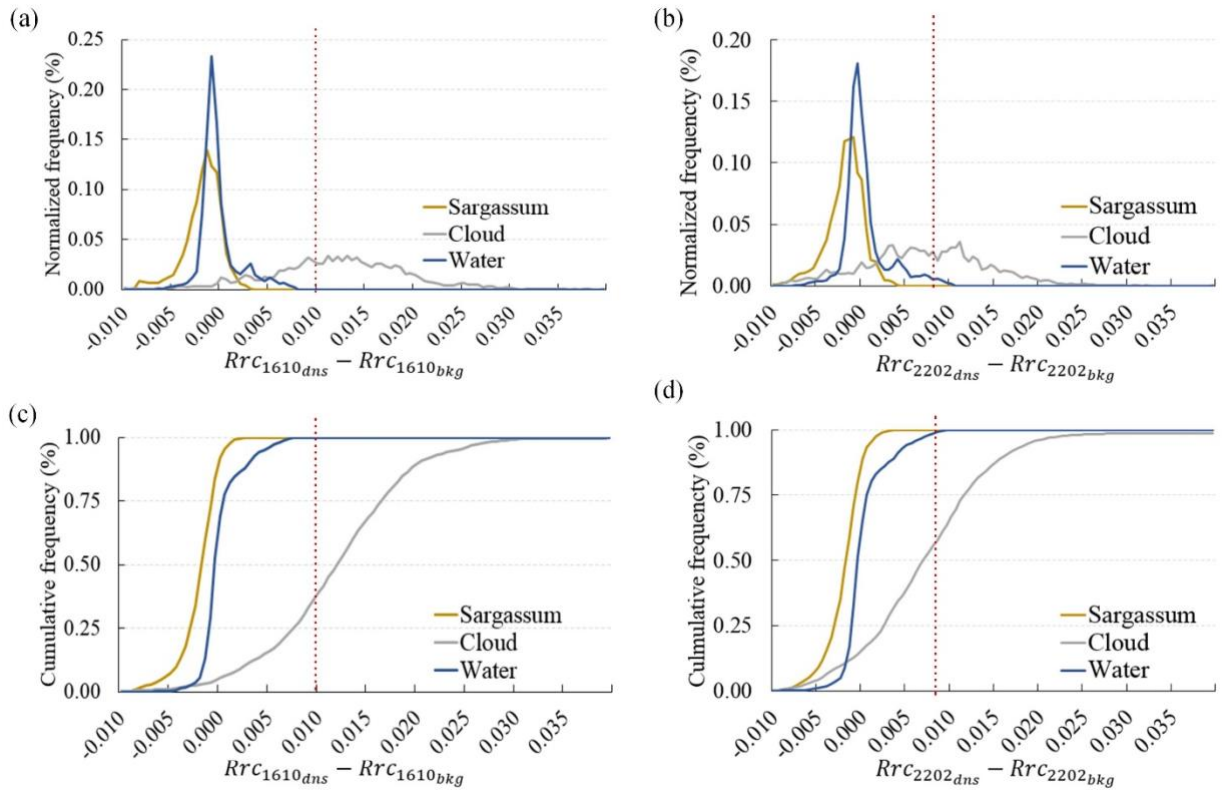

Fig. 4. Normalized and cumulative frequency distributions of Rrc_{1610} and Rrc_{2202} from *Sargassum* pixels, cloud pixels, and water pixels in several regions of interest. (a) and (c): distributions of ($Rrc_{1610_{dns}} - Rrc_{1610_{bkg}}$); (b) and (d): distributions of ($Rrc_{2202_{dns}} - Rrc_{2202_{bkg}}$). The dashed lines mark the selected thresholds for cloud masking (T_{1610} = 0.01 and T_{2202}=0.008).

Although most of the cloud pixels can be effectively identified, some cloud pixels are still missed by the H_SWIR method, especially when clouds are thin or under cloud shadow. These pixels have strong cross-band displacements with high FAI values (Fig. 3d & Fig. 7c). These pixels typically have relative low SWIR reflectance, thus hard to be extracted with the H_SWIR method. However, based on their unique morphological patterns, these pixels can be filtered out using the following TNRD-based denoising model while the real *Sargassum* features are preserved.

2) TNRD-based image denoising

The TNRD model [37] is essentially a convolutional network with trainable linear filters and influence functions, which is used in this study to estimate the noise component from the MSI FAI image, and is then subtracted from the original FAI image to obtain a "clean" FAI image without attenuating the major *Sargassum* features. In Chen and Pock (2016), the synthesized patterns generated with the TNRD model can reproduce similar noise structures as observed on the MSI FAI images.

In this study, the diffusion model was set up with 48 filters of size 7 × 7. The filter number and size were selected to achieve a good compromise between denoising performance and computational cost [37]. We first trained five stages of the TNRD model and then refined the parameters of all five stages through a joint training. The gradient-based L-BFGS algorithms were used for training optimizations during the joint training [46]. The diffusion network structure (the number of filters and filter size) and the number of stages were selected to achieve satisfactory denoising performance with acceptable computational stress [37]. The codes for model training and denoising were downloaded from https://www.dropbox.com/s/8j6b880m6ddxtee/TNRD-Codes.zip?dl=0 [47].

To train the convolutional network to model the typical image artifacts and noises on MSI FAI images, one critical step is to prepare training samples with the corresponding "clean" images and "noisy" images. In the regions with strong noise contaminations, it is often very challenging to manually delineate the real *Sargassum* features, making it difficult to prepare training samples for noisy regions. For denoising tasks, with known noise types, the synthetic noises (such as the Additive White Gaussian noise) are often added to the clean images to create the training images to train the denoising model. Based on this consideration, we selected the MSI FAI images with noisy water pixels (i.e., no *Sargassum*, no clouds) as the known noise sources, and the training images were simulated using these representative noise patterns (including wave induced glint patterns and cloud residuals) and true *Sargassum* features delineated from less noisy *Sargassum*-containing images.

Specifically, to select the typical noise patterns, several FAI images were cropped to 400 × 400 sub-images, from which 496 water images with various wave and cloud residuals patterns were chosen (see examples in Fig. 5b). These "noisy" images were used as the pure noisy components that were superimposed on the delineated true *Sargassum* features to simulate the training "noisy" images. As shown in Eq (3) and Fig. 5a, the clean images were generated by adding the median filtered noise image to the

background subtracted *Sargassum* images, while the corresponding noisy images were generated by adding the original noisy water images. Examples of the simulated training image pairs are illustrated in Fig. 5c. Of the 496 400 × 400 image pairs prepared, 471 were selected to train the TNRD model and 25 were used to evaluate the model performance.

$$FAI_{clean} = FAI_s + FAI_{water\_clean}$$
$$FAI_{noisy} = FAI_s + FAI_{water} \quad (3)$$

Here FAI_{clean} and FAI_{noisy} represent the clean and noisy images, respectively. FAI_S is the *Sargassum* image after subtracting the image background. The FAI_{water_clean} and FAI_{water} are the median filtered noisy water image and the original noisy water image, respectively.

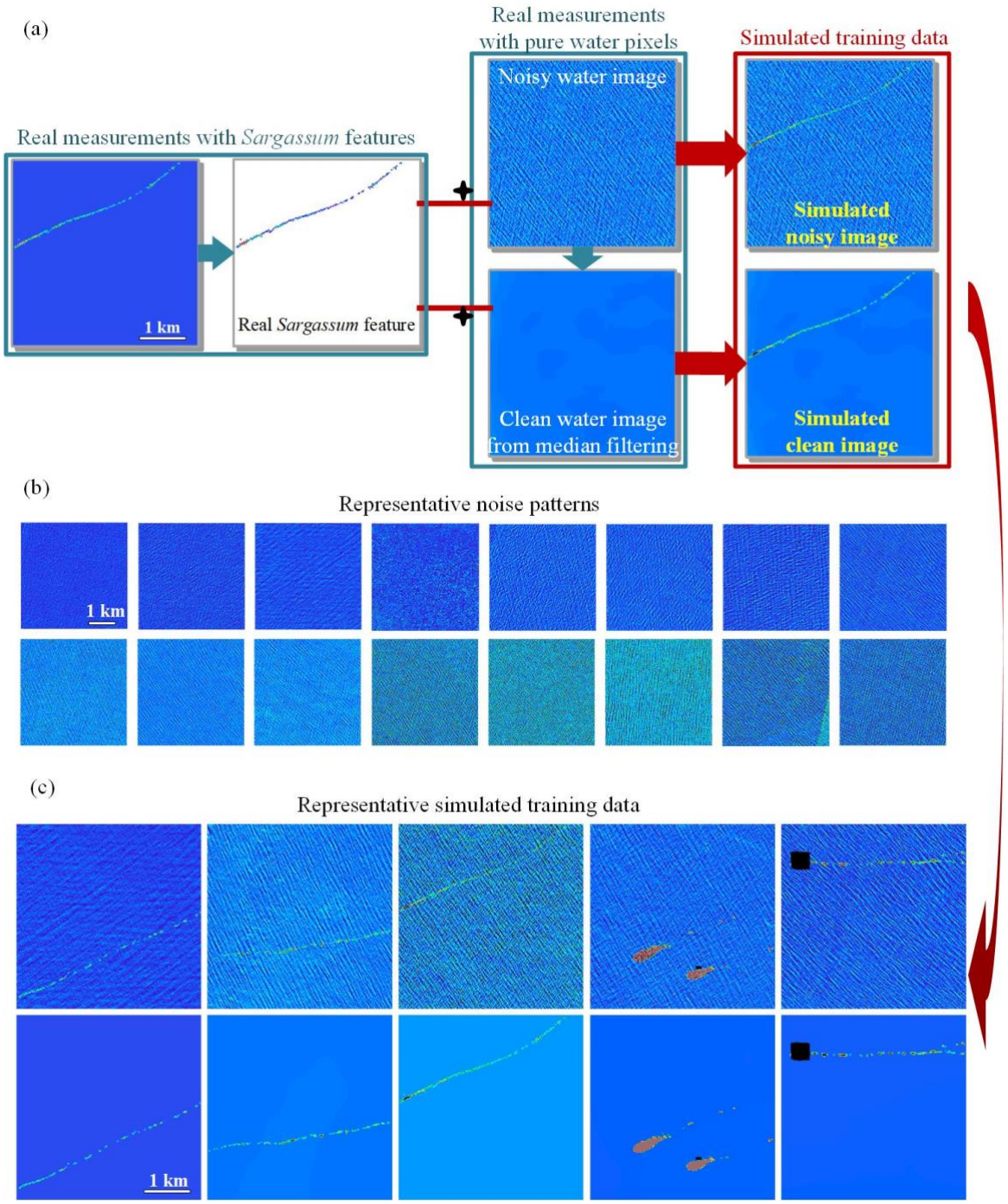

Fig. 5. Training sample preparation and typical noise patterns on the MSI FAI images. (a) shows the process of preparing simulated training data. (b) shows the representative noise. (c) shows examples of the simulated training data prepared using the methods described in (a) and the typical noise patterns illustrated in (b). The upper row in (c) shows the noisy images and the lower row shows the corresponding clean images.

The TNRD-denoised results were compared with those from several popular denoising methods, including Gaussian smoothing, TV filtering, and BM3D [48] approaches. Two image restore quality metrics, the peak-signal-to-noise ratio (PSNR) and the structural similarity index measures (SSIM), were selected to evaluate the denoising results [49]. Higher PSNR and higher SSIM between the denoised image and the "clean" image indicate a better denoising capacity. For both Gaussian smoothing and TV filtering, the parameters with higher PSNR and SSIM were selected in this comparison. For the BM3D implementation, the noise

level was estimated as the standard deviation of the noise component in the test dataset, which was generated by subtracting the clean image from the noisy image. Of the 25 FAI images tested, the mean standard deviation of noise is 0.004. Table 1 summarizes the comparison of the denoising performance of the tested methods.

Of all the tested methods, TNRD shows the highest PSNR and SSIM (Table 1). It also shows better denoising results than other methods from visual inspection (Fig. 6). Both the Gaussian and BM3D denoising methods show less satisfactory performance, with strong smoothing over true *Sargassum* features and with residual wave patterns in the denoised images. Although weak noises can be reduced effectively in the BM3D denoised images, strong repetitive wave patterns can still be visualized. By selecting the optimum weight, the TV filtering method appears to have similar performance as the TNRD method in terms of PSNR and SSIM. However, the watery-effect of feature smoothing as well as residual noise in the TV denoised images still exist (Fig. 6).

TABLE 1. DENOISING PERFORMANCE OF THE TNRD METHOD (THIS STUDY) AND SEVERAL OTHER METHODS.

	Original	**Gaussian**	**BM3D**	**TV**	**TNRD**
PSNR (dB)	26.81	31.89	33.30	36.97	**38.85**
SSIM	0.40	0.91	0.73	0.98	**0.98**

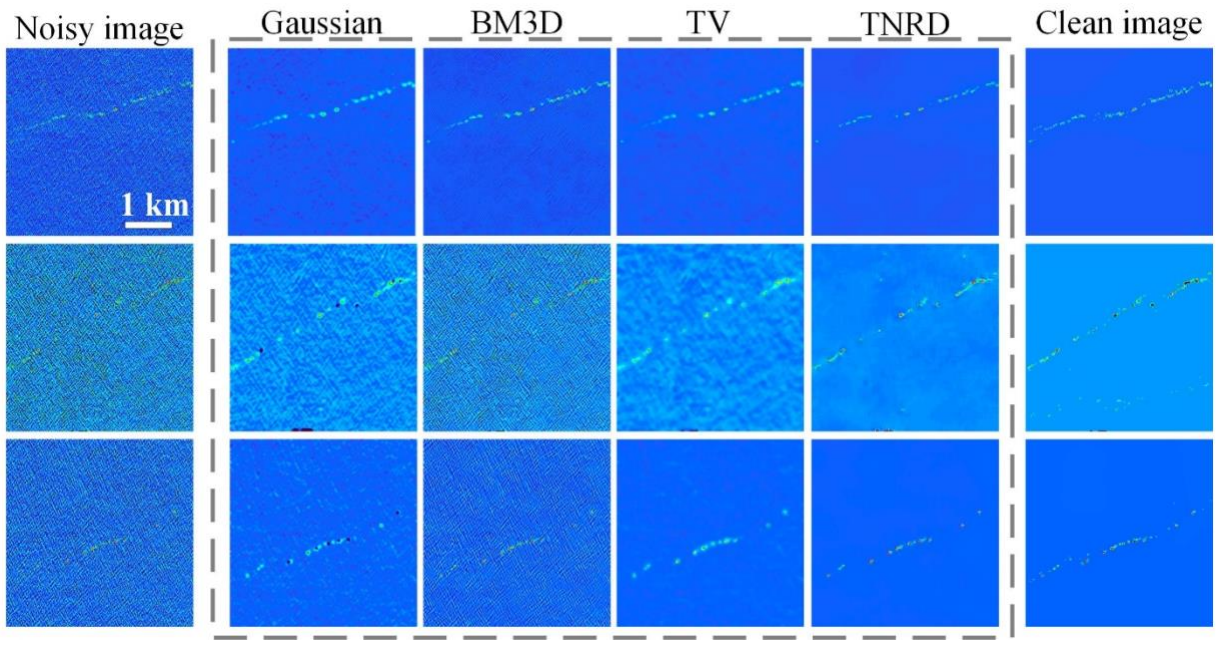

Fig. 6. Performance comparison of different denoise methods. Each column in the dashed rectangle shows the denoised images from one method, with the method annotated on the top. The left-most column shows the noisy images, used as the inputs of the denoise method. The right-most column shows the clean images, used as the "truth" to gauge the performance of the denoise methods.

In addition to better denoising performance, another important advantage of applying the TNRD denoising before *Sargassum* extraction is that the TNRD method can be trained to smooth the cloud residuals, water boundaries, and stripe edges (Fig. 7). During preparation of the training samples, in addition to the noise patterns above, representative residual clouds, boundary features, and stripes ("noisy" images), and their corresponding smoothed results ("clean" images) were also selected. Therefore,

the TNRD denoising method was trained to simulate these image patterns as “noises”. Because of this smoothing effect, the background estimation using median filtering will not create artifacts near those regions with abrupt changes, thus reducing false positive *Sargassum* extraction.

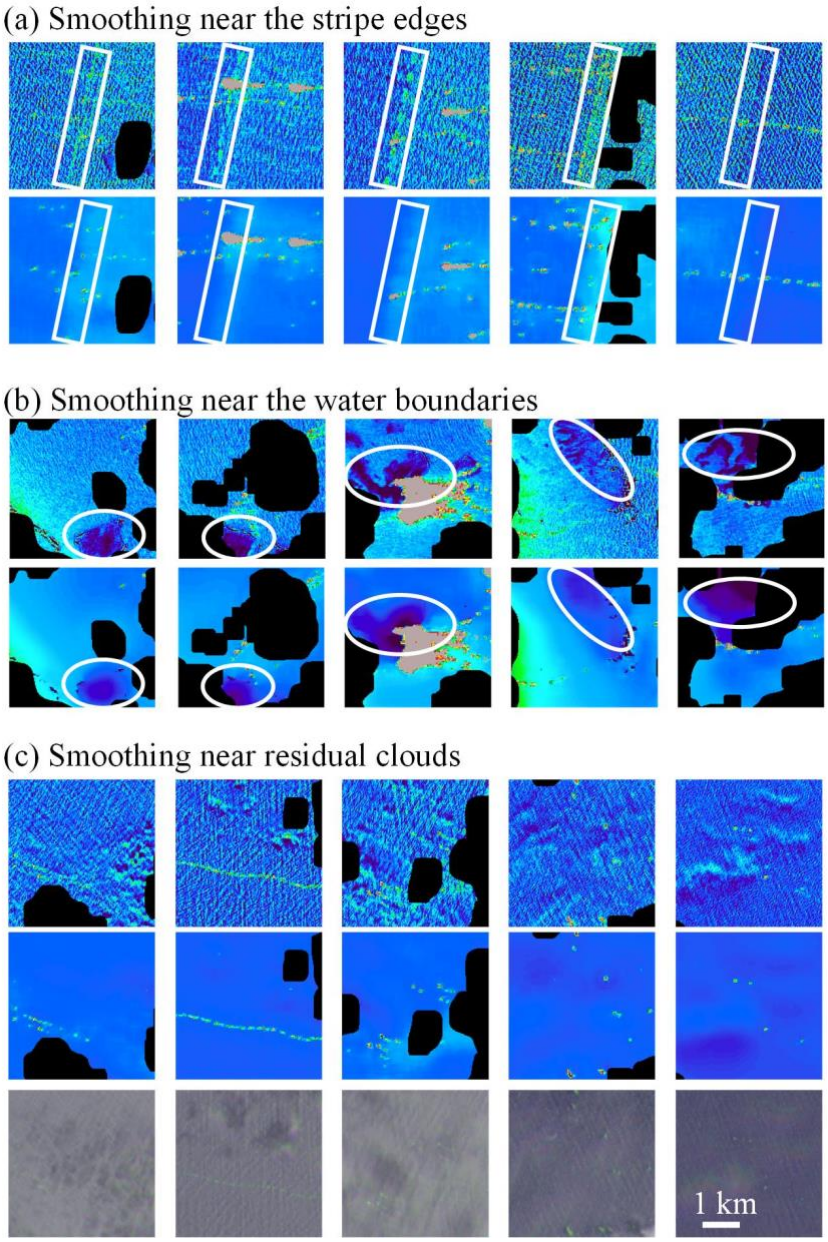

Fig. 7. Smoothing effects over the stripe edges (a), water boundaries (b), and residual clouds (c) after applying the TNRD denoising method. The effects are important in estimating the image background before *Sargassum* feature extraction. The two rows of each sub figure in (a-c) list the original FAI images and the denoised images. The 3rd row in (c) lists the false color RGB images to help visualize cloud and cloud shadow pixels. The white boxes in (a) highlight the regions with stripe noise and the white circles in (b) highlight the water boundaries that are smoothed after denoising. Note that there are almost no other confusing bright features after TNRD denoising.

3) Background estimation and Sargassum extraction

Because Rrc is a result of partial atmospheric correction (i.e., without correcting aerosol effects) and because of the staggered detector configuration [36], the ocean background reflectance can vary within individual MSI FAI images. To extract the local

high FAI values (i.e. from the *Sargassum*-containing pixels) and to quantify the relative *Sargassum* biomass density, the image background variations were estimated through iterative median filtering after H_SWIR cloud masking and TNRD image denoising. The median background estimation was realized using the astropy python package [50-51] (downloaded at https://photutils.readthedocs.io/en/stable/background.html).

The size of the median filtering window (to determine the image background) was selected according to visual inspection of typical size of the *Sargassum* mats or rafts (see section 4.1). In MSI images, *Sargassum* mats and rafts are typically small and they are also aligned coherently in space, thus not requiring a large filtering window to reconstruct the background signal. Additionally, there can be small-scale background changes, especially near the coastal areas (Fig. 7b). Given these considerations, a 10 × 10 window size was applied. In cloud masking process, the background estimation of the SWIR bands used a 200 × 200 window size. This is because reflectance in the SWIR bands from water pixels are usually small and relatively stable across the image. To reduce the impact of abnormal pixels, we also excluded pixels whose absolute differences from the mean were larger than 3 times the standard deviation. This is named as the sigma-clipping process and was run for a maximum of 15 times until convergence.

The estimated ocean background FAI values were then subtracted from the denoised FAI image to derive the locally adjusted FAI values. Because most small noises were smoothed after the TNRD denoising, the standard deviation of each 10 × 10 window was used as the *Sargassum* extraction threshold for that window.

4) Sargassum biomass density quantification

To convert the adjusted FAI values to *Sargassum* biomass densities, FAI-biomass models for S2A and S2B were established based on previous field experiments [6]. Because S2A and S2B have different spectral responses for each band and their radiometric calibrations are also possibly different, the hyperspectral reflectance measurements were first averaged with the S2A/S2B Spectral Response Functions (SRF) for the corresponding wavelengths to derive the FAI values in each group of measurements at a given *Sargassum* density for S2A and S2B separately.

As revealed in the MODIS AFAI-biomass model [6], a linear relationship exists between the S2A/S2B FAI and biomass density when biomass density is low (R^2 = 0.96 and 0.98, N = 7). At higher biomass densities, the biomass density shows a polynomial increase as the FAI value increases (R^2 = 0.96 and 0.96, N = 21). The inflection point occurs at FAI ~0.06, corresponding to *Sargassum* density of 1 kg/m^2. The FAI-biomass model for MSI of S2A and S2B was then established as equations (4) and (5), respectively.

$$\begin{cases} y = 20.65x & (0 < x \le 0.06) \\ y = 24.57\,(x - 0.06)^2 + 41.14(x - 0.06) + 1.24 & (x > 0.06) \end{cases} \quad (4)$$

$$y = 16.06x \qquad (0 < x \le 0.06)$$

$$y = 100.59\ (x - 0.06)^2 + 24.53(x - 0.06) + 0.96 \qquad (x > 0.06) \qquad (5)$$

where x and y represent the FAI values and the modeled *Sargassum* biomass density (kg/m^2). Here Eq. 4 is for S2A while Eq. 5 is for S2B. Fig. 8 shows the relationships between S2A/S2B FAI and *Sargassum* biomass density.

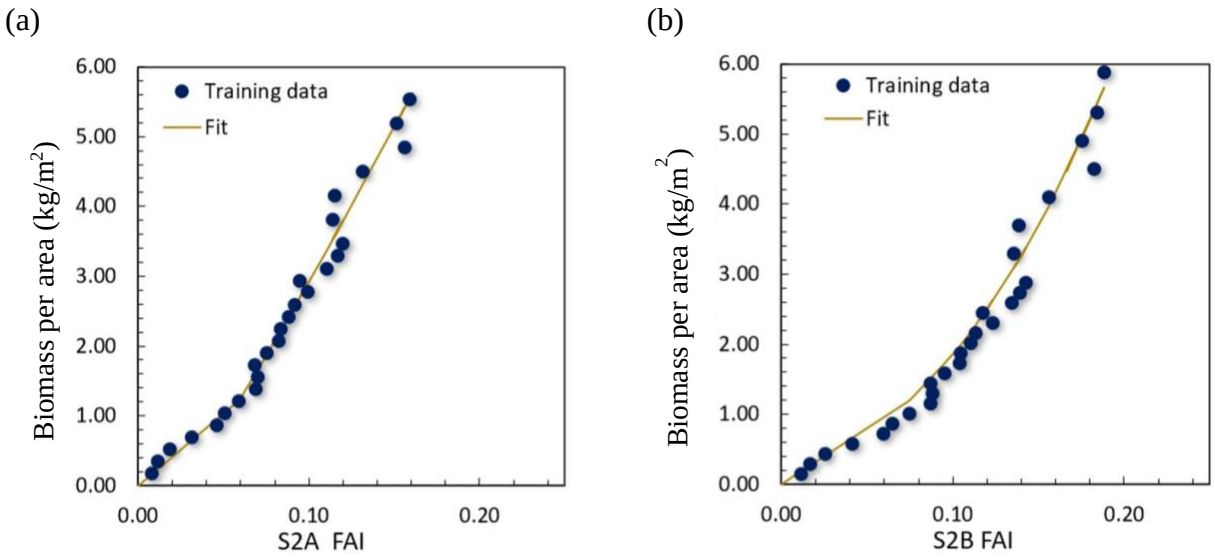

Fig. 8. *Sargassum* biomass density (kg/m^2) versus in situ S2A FAI (a) and S2B FAI (b). The blue dots are the field-measured data used in Wang et al. (2018). The solid line is the model fit using the training data.

Equations 4 and 5 were derived from field measured reflectance, which should be adjusted to account for atmospheric effects when applied to satellite-derived Rrc. Similar to the approach outlined in Hu (2009) and Wang & Hu (2016), simulated Rrc values were derived from the *in-situ* reflectance spectra and variable aerosols and geometries through radiative transfer simulations. The conversion factors modeled between the S2A/S2B FAI and the *in-situ* FAI are listed in Fig. 9 (R^2 = 1.00).

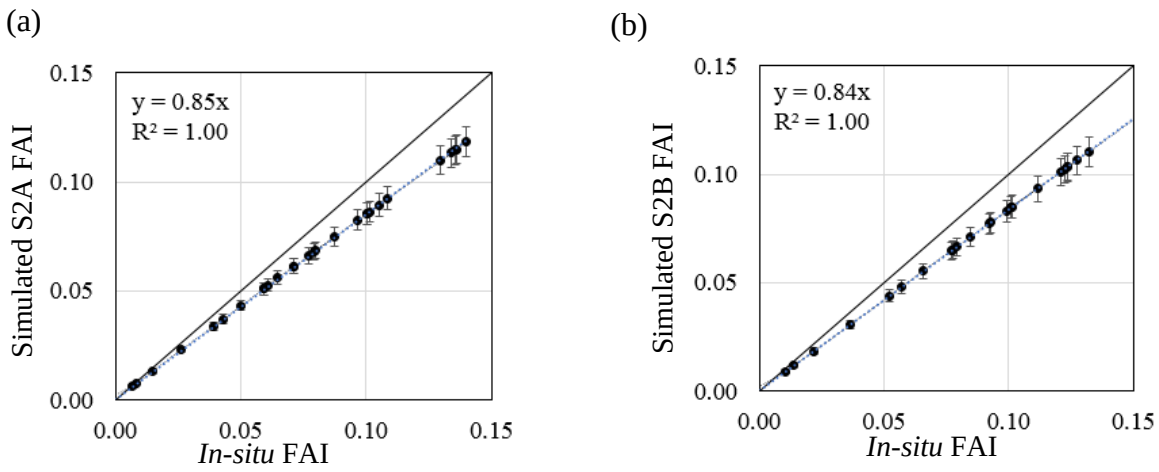

Fig. 9. Simulated S2A FAI (a) and S2B FAI (b) with the aerosol optical thickness at 869 nm, $\tau_a(869)$ = 0.10, averaged under different aerosol types and viewing geometry. The solid line is the 1:1 line and the dashed line is the fitted line. The standard deviations of the simulated FAI are indicated by the vertical error bars. For both S2A and S2B, the simulated FAI is lower than the *in-situ* FAI.

After applying the conversion factors, equations 4 and 5 become:

$$y = 24.29x \qquad (0 < x \leq 0.05)$$

$$y = 24.57\,(1.18x - 0.06)^2 + 41.14(1.18x - 0.06) + 1.24 \qquad (x > 0.05) \tag{6}$$

$$y = 19.12x \qquad (0 < x \leq 0.05)$$

$$y = 100.59\,(1.19x - 0.06)^2 + 24.53(1.19x - 0.06) + 0.96 \qquad (x > 0.05) \tag{7}$$

Note that these equations are applied directly to MSI FAI values of the delineated *Sargassum* features after cloud masking, TRND denoising, and background subtraction. In the 10-m resolution MSI images, many *Sargassum*-containing pixels show FAI values above the linear response range (results section C). Therefore, it is important to combine the linear and non-linear equations (equations 6 and 7) to convert FAI to biomass density.

III. Results

A. Sargassum extraction accuracy on MSI images

The proposed approach was tested over 10 representative MSI FAI images (tile: T20PNC) collected in 2018. The estimated biomass densities after automatic extraction were compared with the delineated "ground truth" [52] to estimate the overall accuracy (F-score, [53]). The "ground truth" data were prepared using a semi-automatic IDL GUI designed to extract the brighter features with selected thresholds and morphological constraints [52].The extraction results using the same workflow with no denoising or with TV filtering (weight = 0.02, the optimum weight selected in section 2.3.2) were also generated for comparison.

As shown in Table 2, without denoising, the false positive rate is extremely high, possibly due to the strong noises and various confusing features. Applying TV filtering in the procedure preserved most of the *Sargassum*-containing pixels (with 6% false negative rate) with false positive rate reduced significantly, yet there are still large detection errors (~76% false positives). With the TNRD denoising, the false positive rate is reduced significantly to ~7%, and the *Sargassum* extraction precision is >90% in most cases. However, the TNRD denoising process also inevitably smoothed some weak features, as indicated by a higher false negative rate and lower recall. The 20% false negative rate suggests that 20% of the *Sargassum*-containing pixels may not be extracted after TNRD denoising. This is because many weak *Sargassum* features can be easily confused with water signals (Fig. 1) and even manual delineation is difficult. Overall, the proposed *Sargassum* extraction approach showed an extraction accuracy of ~86%. Considering that most of the undetected *Sargassum* features (i.e., false negative detection) are of low density (i.e., very weak FAI signals) and the extraction precision is >90%, this approach is regarded to be promising for automatic *Sargassum* feature extraction and biomass estimation.

TABLE 2. COMPARISON OF THE *SARGASSUM* EXTRACTION ACCURACY USING DIFFERENT DENOISING METHODS ON TEN SELECTED MSI FAI IMAGES. FOR THE RESULTS WITH NO DENOISING, THE EXTRACTION THRESHOLDS WERE SELECTED AS TWICE THE STANDARD DEVIATION OF THE 10×10 WINDOW.

Denoising methods	False positive	False negative	Precision	Recall	F score
No denoising	**1481%**	**0%**	**6%**	**100%**	**12%**
TV filtering	**76%**	**6%**	**56%**	**94%**	**70%**
TNRD denoising	**6%**	**20%**	**93%**	**80%**	**86%**

B. Comparison of Sargassum biomass densities derived from MSI and MODIS

With higher spatial resolution, it is expected that MSI should be capable of detecting more small-scale *Sargassum* features than MODIS, thus resulting in higher biomass estimates for common cloud-free and noise-free regions. To verify this speculation and understand their difference, 13 quasi-simultaneous images collected by MSI and MODIS within 30-minutes were selected (Table 3). Fig. 10 shows four examples of the match-up observations from these two sensors.

TABLE 3. COMPARISON OF *SARGASSUM* BIOMASS DERIVED FROM QUASI-SIMULTANEOUS MODIS AND MSI OBSERVATIONS IN COMMON AREAS AND IN ENTIRE SCENES FROM TILE T20PQB. HERE THE COMMON AREA REFERS TO THE AREA WHERE BOTH MODIS AND MSI HAVE VALID OBSERVATIONS (I.E., CLOUD-FREE AND NOISE-FREE).

Date	MODIS sampling time (GMT)	MSI sampling time (GMT)	*Sargassum* biomass in the common area (kilotons)		*Sargassum* biomass in the entire scene (kilotons)	
			MODIS	MSI	MODIS	MSI
2018/05/09	14:55	14:37	0.55	0.14	0.73	2.91
2018/05/24	14:10	14:37	1.36	0.16	1.47	7.74
2018/05/29	14:30	14:37	14.96	2.99	15.29	13.74
2018/06/18	14:05	14:37	2.34	2.61	2.83	10.97
2018/06/23	14:25	14:37	0.00	0.01	0.00	6.07
2018/07/18	14:20	14:37	0.61	0.12	0.61	5.46
2018/07/23	14:35	14:37	1.57	1.11	1.66	3.66
2018/08/12	14:10	14:37	0.56	0.56	0.57	1.01
2018/08/17	14:30	14:37	0.89	0.21	0.90	1.53
2018/09/11	14:25	14:37	1.97	3.05	2.18	8.87
2018/10/16	14:55	14:37	0.00	0.01	0.00	0.03
2018/10/26	13:55	14:37	0.00	0.00	0.00	4.24
2018/12/05	14:40	14:37	0.10	0.00	0.10	0.05

Surprisingly, the MSI-derived biomass can be both higher and lower than MODIS-derived biomass. The former is easy to understand because MSI can observe small-scale *Sargassum* features that are difficult to observe from MODIS images (Fig. 10, region 3-4). In contrast, the latter is rather difficult to understand. A close inspection of the detection results for regions 1-2 of Fig. 10 indicate that the lower estimation from MSI is due to the false negative detection of many small *Sargassum* patches, which spread evenly over a large noisy region. Such small patches, when integrated together, resulted in a detectable signal in the corresponding MODIS images (Fig. 10, region 1-2). Indeed, after aggregating the 10-m MSI pixels into 1-km resolution pixels, the 1-km MSI pixels are able to detect some of the "missing" small features (Fig. 10, region 1-2). However, the same aggregation also led to underestimation over the dense *Sargassum* features (Fig. 10, regions 3-4), therefore cannot be applied universally to reduce false-negative detection rate.

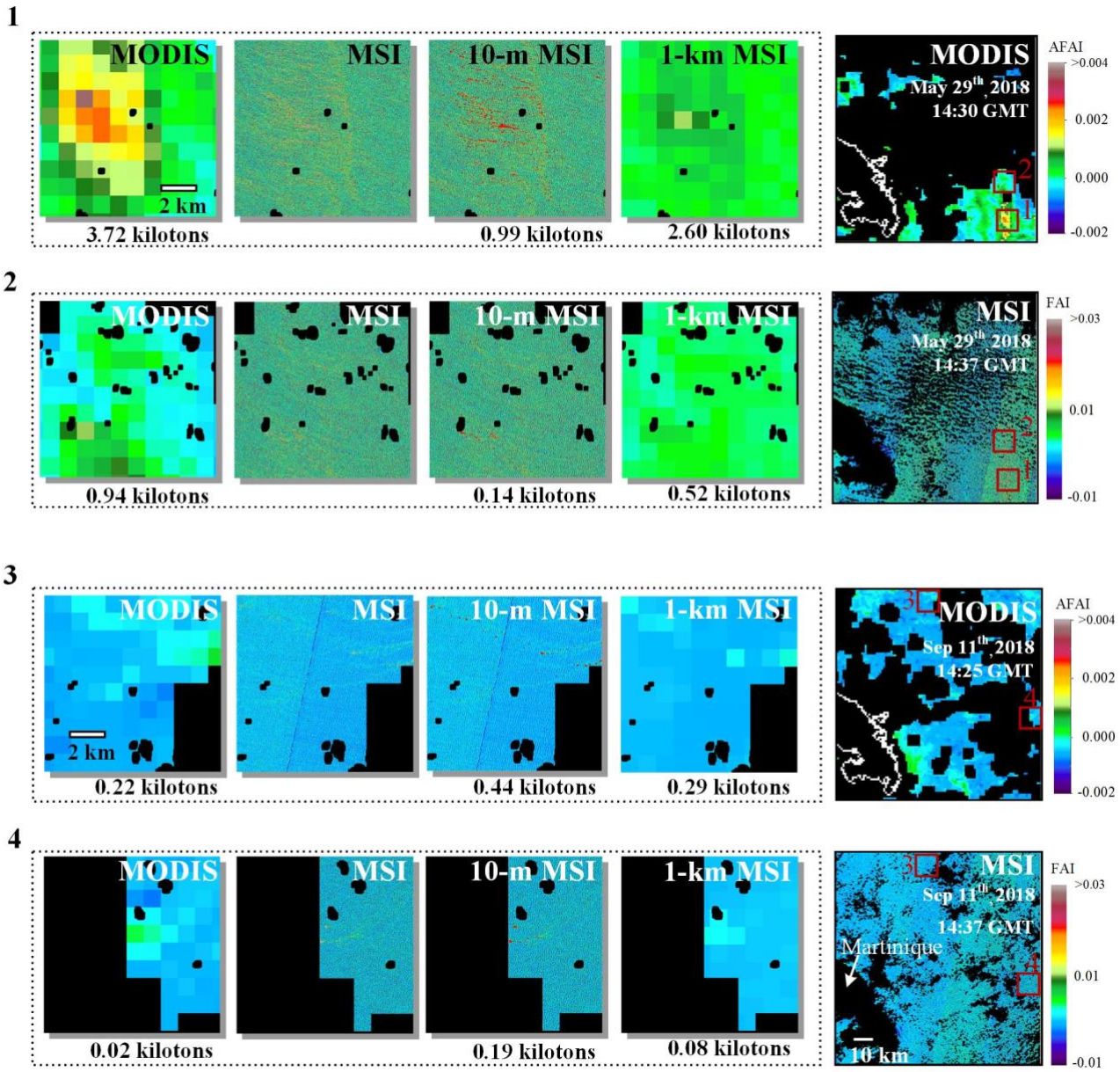

Fig. 10. Examples of the quasi-simultaneous MODIS AFAI (1-km resolution) and MSI FAI (10-m resolution) observations. The MODIS scenes are cut to match the MSI coverage (14.4˚ N to 15.4˚ N and 61.1˚ W to 60.1˚ W, right column). The white color and black color represent the coastline and no valid observations, respectively. Four small regions (marked by the numbered red boxes on the right panels) are enlarged to show the corresponding features The extracted *Sargassum*-containing pixels are marked in red on the 10-m MSI subimages. The 1-km MSI subimages show the aggregated MSI pixels (100 × 100 10-m MSI pixel = 1 1-km MSI pixel). The extracted total *Sargassum* biomass in the common area for each box is listed below the corresponding images. Note that although the cloud patterns are similar, the MSI cloud mask is much smaller than MODIS cloudmask because of the finer spatial resolution of MSI.

Despite some false negative detections as shown in Fig. 10 (regions 1-2), MSI generally provides more valid observations than the corresponding MODIS because of the smaller cloud cover (Fig. 10 & 11), leading to higher chance of "seeing" *Sargassum* features. This effect has been demonstrated by comparing MODIS 250-m and MODIS 1-km observations over the GOM [27]. Indeed, in almost all 13 cases of Table 3, MSI observed higher amount of *Sargassum* than MODIS over the entire MSI sub-image coverage (last two columns of Table 3, as opposed to the columns corresponding to the common area).

The improved valid observations in individual MSI images over near-simultaneous MODIS images can be clearly seen in the

example of Fig. 11. For the coverage of the entire image, the total "observable" area from the MSI image is 6630.5 km^2 while from the MODIS image is 1045.8 km^2. Furthermore, MSI can provide valid observations in nearshore waters where MODIS capacity is compromised. Fig. 11 shows that the MSI detected *Sargassum* mats and rafts are very close to shore (20 m from the shoreline). This is of critical value for local management in terms of mitigation of adverse impacts of *Sargassum* beaching.

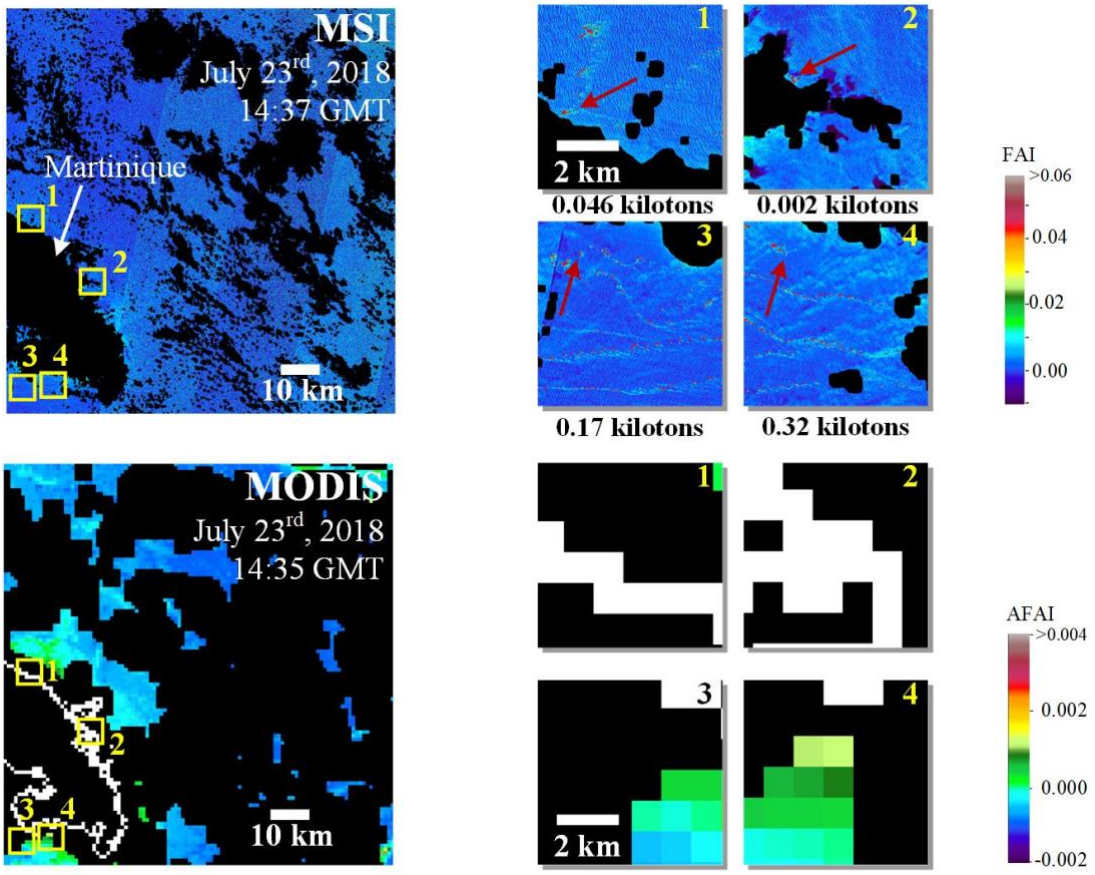

Fig. 11. Comparison of quasi-simultaneous MODIS and MSI observations near the coast of Martinique in the CS (14.4˚ N to 15.4˚ N and 61.1˚ W to 60.1˚ W). Four subimages were selected (highlighted in the yellow boxes in the left panel and enlarged in the right panel). The extracted *Sargassum* pixels in the MSI images are marked in red and the total extracted *Sargassum* biomasses are listed below each MSI sub-image. The red arrows mark the *Sargassum* pixels extracted near the shoreline. The total observable areas are 6630.5 km^2 from MSI and 1045.8 km^2 from MODIS.

For continuous monitoring and assessment, the improved coverage in individual MSI images (as compared with near-simultaneous and co-located MODIS images) is compensated by the MSI 5-day revisit frequency (as compared with daily MODIS revisits). For all MSI and MODIS images collected in 2018 covering the same region shown in Fig. 10, the average daily percent valid observations (DPVOs, see definitions in Feng and Hu, 2016 [54]) are ~ 9% and 20% for MSI and MODIS, respectively. This indicates that, on average and for a random water location, every 11 days there is a valid MSI observation and every 5 days there is a valid MODIS observation (after combining both Aqua and Terra). Despite this difference (as well as the differences in *Sargassum* estimates from individual images), the total integrated *Sargassum* biomass on an average day in 2018 is very similar between MSI and MODIS observations (Fig. 12), suggesting consistency between the two independent observations when relatively long-term, large-scale statistics are to be assessed.

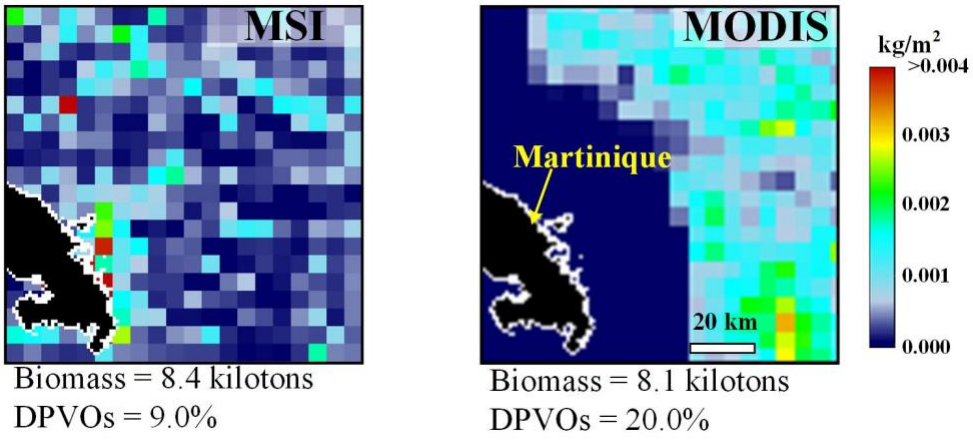

Fig. 12. The annual mean *Sargassum* biomass density derived from MSI (left) and MODIS (right) over T20PQB near Martinique in 2018. Twenty-eight (28) S2A images and thirty (30) S2B images with <80% cloud cover were used to generate the statistics. The corresponding total *Sargassum* biomass and the mean DPVOs (averaged across of the valid grids) are listed below each image. The images cover the area from 14.4˚ N to 15.4˚ N and 61.1˚ W to 60.1˚ W. The total *Sargassum* biomass is for an average day during 2018. Note that the nearshore pixels on MODIS were treated as no observations due to the limitations of these coarse-resolution data.

C. Size, biomass, and morphology of individual Sargassum mats/rafts observed from MSI images

Because of the mixed pixels, the 10-m spatial resolution of MSI enables estimates of *Sargassum* size of individual mats/rafts even much smaller than a pixel size (i.e., 100 m^2). Here, the statistics were generated from the *Sargassum*-containing pixels detected from the 58 MSI images used in section B (collected from tile T20PQB during 2018). Of all *Sargassum*-containing pixels, over 95% contain < 1.71 kg/m^2 of *Sargassum* within each pixel (or < 171 kg/pixel) (Fig. 13a). The highest density is ~18.7 kg/m^2 (or 1,866 kg in one pixel), well above the mean density used to convert areal coverage to biomass density from MODIS coarse-resolution pixels (3.34 kg/m^2, Wang et al, 2018). From the corresponding MODIS AFAI images, signals from these dense *Sargassum* mats are linearly mixed with the water signal over the large MODIS pixels, resulting in underestimation of the actual *Sargassum* biomass. However, 99% of the *Sargassum*-containing pixels have < 329 kg/pixel, indicating that such mixing-induced underestimation in MODIS images is rare. In reality, *Sargassum* mats/rafts can be much smaller than reported here, and some of them are part of the ~20% false negative detection. Because they are lower than the detection limit, their impact on the total biomass may be minimal.

In 1-km MODIS AFAI images, *Sargassum* rafts often appear as elongated, spatially continuous features with variable sizes, stretching up to hundreds of kilometers in length. In the 10-m MSI FAI images, it is very rare to observe such large continuous *Sargassum* features. Rather, smaller rafts are often aligned due to winds and Langmuir circulations. To estimate the typical size and shape of these MSI-observed *Sargassum* features, we analyzed the pixel coverage (not weighted by *Sargassum* densities within individual pixels) of the extracted *Sargassum* features from the 58 MSI images used in section B.

As *Sargassum* typically form elongated weed-lines with a long “tail”, the extracted *Sargassum* patches were first eroded using a 3×3 window to break the “tails” to better estimate the typical sizes of the aggregated patches. The patches were then dilated

outward using the same window size to reconstruct the features. From this analysis, the largest pixel coverage measured in T20PQB in 2018 is ~0.8 km^2, while the mean size is ~2300 m^2 (Fig. 13c). This suggest that under the average conditions the effective width of the *Sargassum* rafts should be < 40-50 meters (this is the extreme case when the length/width ratio equals to 1), corresponding to 4-5 10-m MSI pixels.

To quantify the length of the *Sargassum* rafts, a morphological close operation was applied to the extracted *Sargassum*-containing pixels to connect the nearby *Sargassum* features. The major axis length of the connected features was then determined as the effective length of each individual *Sargassum* mat [55]. From the 58 MSI images measured, the mean *Sargassum* feature length is ~76 m, while the maximum length is ~6.5 km (Fig. 13d). The mean length/width ratio is ~3, but the maximum ratio can reach ~100 (Fig. 13f), consistent with the field observations that *Sargassum* often forms elongated features in the open ocean [9].

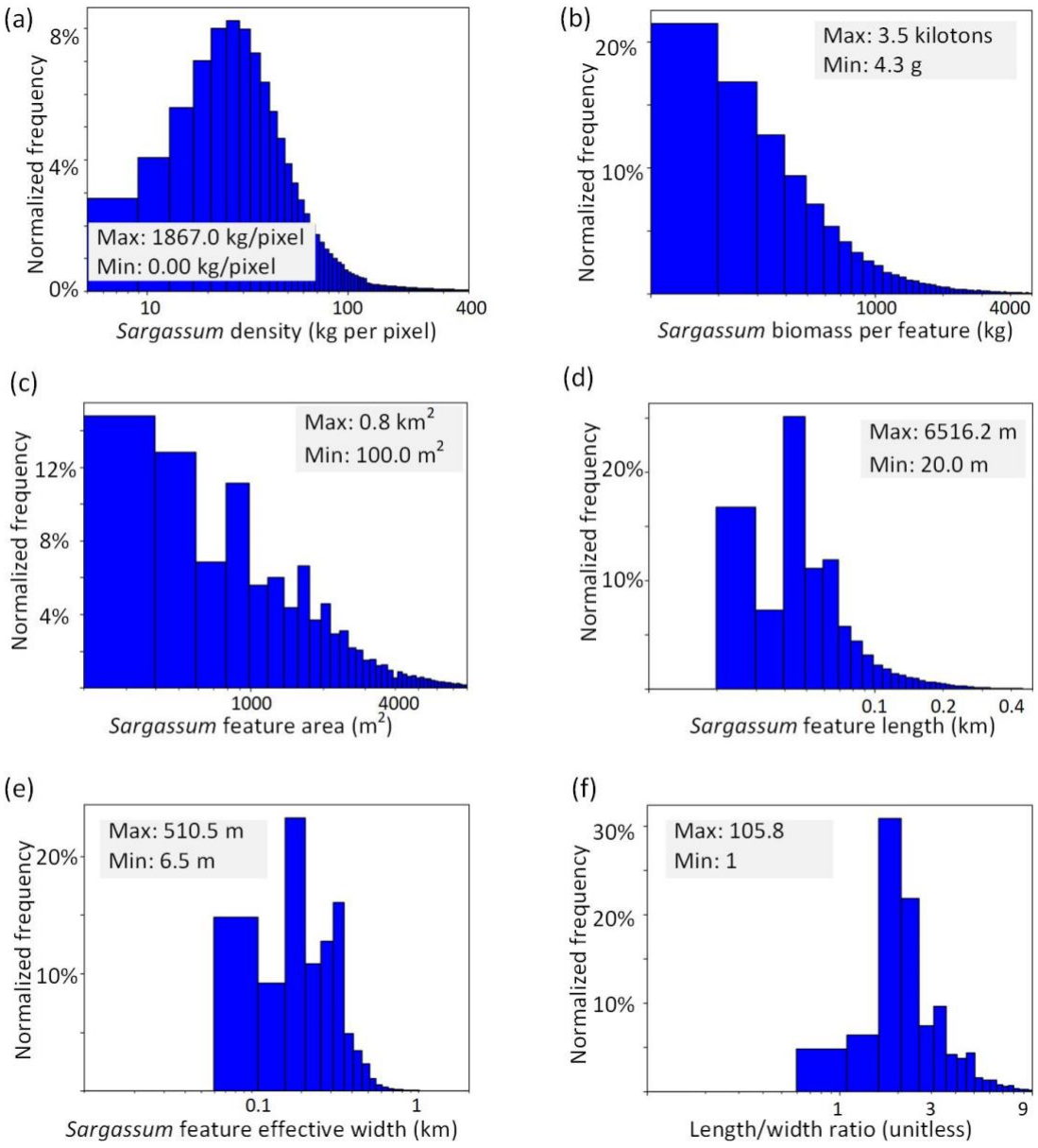

Fig.13. Distributions of normalized frequency of *Sargassum* biomass density (a), total biomass per feature (b), *Sargassum* feature area (c), length (d), width (e), and length/width ratio (f) derived from the *Sargassum*-containing pixels extracted from 58 MSI images (T20PQB) in 2018. The incremental step in these frequency distribution graphs from (a) to (f) are 0.04 kg/m^2, 100 kg, 100 m^2, 10 m, 5 m, and 0.5, respectively. In (a), 95% of the pixels have density lower than 171 kg/pixel, and 99% of the pixels have density lower than 329 kg/pixel.

IV. Discussions

A. Strengths and weakness of the proposed approach

Unlike machine learning approaches such as neural networks, the proposed approach is based on physical principles behind the spectral difference of various image features (*Sargassum*, water, clouds, image noise), with explicit rules to mask clouds and other noises and to delineate *Sargassum*-containing pixels. Therefore, not only are the rules easy to understand, but reasons leading to failures are easy to track down. Furthermore, the approach also uses spatial information (in addition to spectral information) to

distinguish *Sargassum* signals from other confusing features. This is particularly important for MSI because of its high spatial resolution and inconsistent sampling time between different spectral bands. Such "noise" contamination can be induced by ocean waves and residual clouds that do not show conspicuous spectral difference (Fig. 1c). Although their spectra may be similar to *Sargassum*-containing pixels, the spatial patterns of ocean wave-induced glints and cloud residual signals are consistent and different from the *Sargassum* features, thus a well-trained TNRD denoising model can successfully remove most of these "noises" based on their spatial characteristics. This is similar to the use of spatial information to detect macroalgae using Geostationary Ocean Color Imager (GOCI)imagery [56]. Therefore, future algorithm development efforts for other high-resolution sensors may use both spectral and spatial information to improve accuracy.

One limitation of the approach, on the other hand, is 20% false-negative detection due to weak *Sargassum* signals. Although this limitation will not make a big impact on the biomass estimates because the "missed" pixels contain only small amount of *Sargassum*, it will lead to errors when *Sargassum* presence/absence is to be predicted. Such a limitation is partially due to the inherent limitation of the sensor itself (i.e., pixel size, SNR, [45]) because small *Sargassum* clumps commonly observed in the field [9, 57], typically in the size of tens of centimeters, can simply not be detected by a 10-m resolution sensor regardless of the detection approaches. On the other hand, the limitation may also be due to the approach itself, where future efforts may be devoted to "recover" the "missed" pixels with weak *Sargassum* features. Nevertheless, because the undetected *Sargassum* features are associated with low biomass densities, failing to report these features should have relatively small impact on mitigation efforts in response to beaching events.

Recently, deep-learning approaches of the ERISNet and other deep convolutional neural networks have also been applied to extract *Sargassum* and *Ulva prolifera* features on various remote sensing imagery [58-59]. In follow-on studies, improved deep learning algorithms could be explored on whether they can further improve the performance of the current approach, especially on recovering the weak *Sargassum* features while retaining the same low false-positive detection rate.

B. Near real-time applications

For management purpose, *Sargassum* imagery data products should be generated and made available to the user community immediately after the satellite overpass. While the low-level MSI data are usually provided by the USGS within 1-day of the satellite overpass, data processing time is also a factor to consider.

In this study, training the TNRD denoising model with 471 400×400 sample images for 300 L-BFGS iterations took ~318 hours. This was conducted using the Matlab implementation on a server with 24 CPUs (Intel(R) Xeon(R) CPU E5-2650 v4 @ 2.20GHz) and with 12 parallel threads. Table 4 summarizes the average run time of each step on one MSI image (10000 × 10000 pixels) on a server with 39 CPUs (Intel(R) Xeon(R) CPU E5-2660 v3 @ 2.60GHz). The TNRD denoising process took ~11 minutes, slightly

shorter than the time needed for generating the H_SWIR cloud mask on the two SWIR bands (~16 minutes). The ocean background estimation took ~7 minutes. In total, the *Sargassum* extraction time needed for each MSI FAI image of 10000×10000 pixels is ~33 minutes. The training and processing times are both expected to be improved on the GPU implementation [37]. Considering that generating Rrc data from L1C MSI image of the same size using ACOLITE typically takes >30 minutes, the total end-to-end processing time from L1C to biomass estimation is about 1 hour per image, sufficient for near real-time applications.

TABLE 4: APPROXIMATE RUN TIME OF PROCESSES USED IN THE SARGASSUM EXTRACTION APPROACH. THE RUN TIME IN EACH STEP IS THE AVERAGE TIME USED TO PROCESS ONE MSI IMAGE OF 10000 × 10000 PIXELS (10 IMAGES IN TOTAL), ON A SERVER WITH 39 CPUS (INTEL(R) XEON(R) CPU E5-2660 V3 @ 2.60GHZ).

Steps	**TNRD denoising**	**Cloud masking**	**Background estimation with a 10×10 window**
Run time	651 seconds	475 seconds × 2	406 seconds

The real limitation of MSI in its near real-time applications is its low revisit frequency (once every 5 days). Although the relatively high resolution leads to less cloud coverage than from coarse-resolution sensors, the 4-day gap leads to simply no data. Before new MSI-like sensors are put in orbit, a temporary solution is to combine other high-resolution sensors such as OLI from Landsat-8.

With the 30-m spatial resolution, the Landsat-8 OLI images also suffer from similar challenges of noise contamination from clouds and ocean waves when automate *Sargassum* extraction is desired. Therefore, the applicability of the proposed *Sargassum* extraction approach is tested over Landsat-8 FAI images.

Similar to the approach for MSI, a TNRD denoising model was trained using the simulated noise patterns to reduce noise from Landsat-8 FAI images. In this preliminary evaluation, 343 representative sub-images, each containing 400 × 400 pixels, were selected from 2 Landsat-8 FAI images. Similar cloud masking method based on the enhanced SWIR reflectance was used to mask cloud pixels. Fig. 14 shows an example of the *Sargassum* extraction results.

From visual inspection, *Sargassum* extraction after the cloud masking and TNRD denoising from Landsat-8 images appears satisfactory. The extraction accuracy was evaluated by comparing the automatic extraction with those from manual delineation (regarded as the "truth"). After weighting the *Sargassum*-containing pixels by their biomass densities, which were derived from the field-based model to convert Landsat-8 FAI to biomass density, the overall *Sargassum* extraction accuracy reached ~93%, with 6% false positives and 8% false negatives from the tested Landsat-8 FAI image. Due to the larger pixel size and higher SNR of Landsat-8 OLI data [45], the "noise" magnitudes due to ocean waves are weaker than those in MSI images, resulting in lower false negatives. Although further testing is required, the preliminary results clearly demonstrate the potentials of the proposed *Sargassum* extraction approach to other similar sensors. Once confirmed, we expect to implement the approach to process both MSI and Landsat-8 images for selected regions and make the end results available to the user community in near real-time through the existing *Sargassum* Watch System (SaWS, [15]; https://optics.marine.usf.edu/projects/saws.html). Currently, *Sargassum*-relevant

data products from coarse-resolution sensors such as MODIS and VIIRS are already available and updated daily through SaWS for the GOM and CS. Inclusion of the finer-resolution MSI and Landsat-8 imagery will significantly enhance the system's capacity in monitoring and tracking *Sargassum* in coastal and nearshore waters.

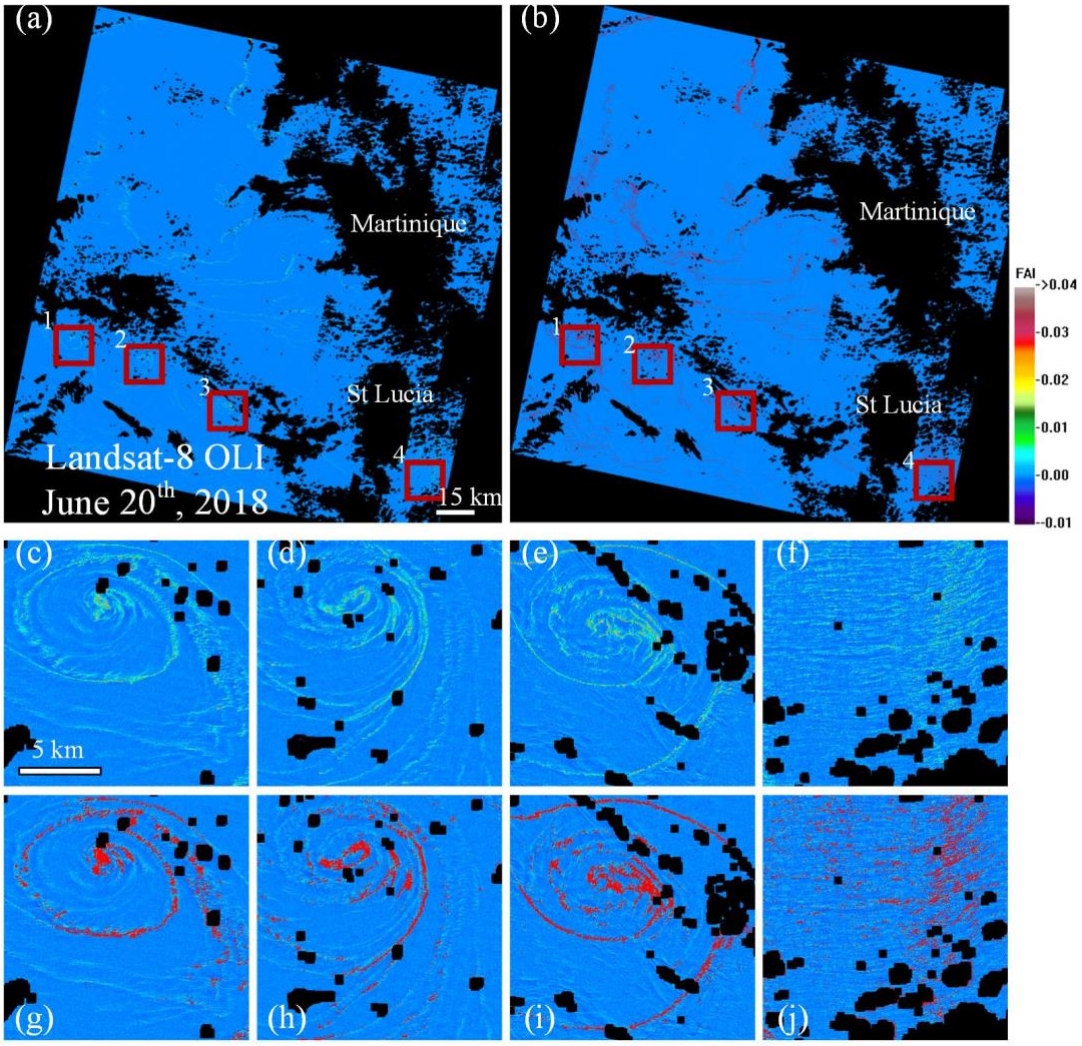

Fig. 14. *Sargassum* extraction results from Landsat-8 observations (image taken on June 20th, 2018 near Martinique, from 13.5˚ N to 15.5˚ N and from 62.5˚ W to 60.5˚ W). (a) shows the original FAI image; (b) shows the correpsonding *Sargassum* extraction results with the extracted *Sargassum*-containing pixels marked in red. Four subimages (shown in red boxes in (a) and (b)) are enlarged to examine the extraction results. Here, the large-scale background variations were subtracted from the Landsat-8 FAI images for better visuallization. The cloud masking thresholds are identical to those applied to MSI images. Note that the *Sargassum* features appear to be "dragged" by the cyclonic eddy (enlarged in (c-e) and (g-i)) to accumulate in the eddy center.

V. Conclusions

A fully automatic workflow has been designed to use the high-resolution MSI data to extract *Sargassum* features in coastal and nearshore waters. The success of the approach is mainly due to the TNRD denoising model, which is trained with representative and realistic noise patterns to reconstruct and remove the various noise patterns before conducting the *Sargassum* extraction process. The TNRD model shows improved performance as compared with several other traditional denoising approaches in

removing the various MSI noise patterns. Application of the automatic approach shows an overall *Sargassum* extraction accuracy of ~86%. Although the false negative rate is ~20%, these undetected *Sargassum*-containing pixels have lower densities than the detected *Sargassum*-containing pixels, thus having minimal impacts on the total biomass estimates and on management actions against major beaching events. On the other hand, the *Sargassum* extraction precision is >90%, suggesting that most of the extracted *Sargassum* features are real. The approach also shows applicability to Landsat-8 OLI FAI images, with an overall extraction accuracy of 93%. We expect to implement this approach to generate both MSI and OLI *Sargassum* extraction images in near real-time for selected coastal regions and share them through the existing *Sargassum* Watch System.

ACKNOWLEDGMENT

This work was supported by the U.S. NASA Ocean Biology and Biogeochemistry program NNX14AL98G, NNX16AR74G) and Ecological Forecast Program (NNX17AE57G), NOAA RESTORE Science Program (NA17NOS4510099), the JPSS/NOAA Cal/Val project (NA15OAR4320064), and Sackett Prize for Innovative Research. We thank the two reviewers for their useful comments.

REFERENCES

[1] J. Gower, E. Young, and S. King, "Satellite images suggest a new *Sargassum* source region in 2011," *Remote sensing letters*, vol. 4, pp. 764-773, 2013.
[2] V. Smetacek and A. Zingone, "Green and golden seaweed tides on the rise," *Nature*, vol. 504, pp. 84-88, 12/05/print 2013.
[3] M. Wang and C. Hu, "Mapping and quantifying *Sargassum* distribution and coverage in the Central West Atlantic using MODIS observations," *Remote Sensing of Environment*, vol. 183, pp. 350-367, 2016.
[4] M. Wang and C. Hu, "Predicting *Sargassum* blooms in the Caribbean Sea from MODIS observations," *Geophysical Research Letters*, vol. 44, pp. 3265–3273, 2017.
[5] M. Wang and C. Hu, "On the continuity of quantifying floating algae of the Central West Atlantic between MODIS and VIIRS," *International Journal of Remote Sensing*, vol. 39, pp. 3852-3869, 2018.
[6] M. Wang, C. Hu, J. Cannizzaro, D. English, X. Han, D. Naar, *et al.*, "Remote sensing of *Sargassum* biomass, nutrients, and pigments," *Geophysical Research Letters*, vol. 45, pp. 12,359-12,367, 2018.
[7] M. Wang, C. Hu, B. B. Barnes, G. Mitchum, B. Lapointe, and J. P. Montoya, "The great Atlantic *Sargassum* belt," *Science*, vol. 365, pp. 83-87, 2019.
[8] J. Gower and S. King, "The distribution of pelagic *Sargassum* observed with OLCI," *International Journal of Remote Sensing*, pp. 1-11, 2019.
[9] A. Ody, T. Thibaut, L. Berline, T. Changeux, J.-M. André, C. Chevalier, *et al.*, "From *In Situ* to satellite observations of pelagic *Sargassum* distribution and aggregation in the Tropical North Atlantic Ocean," *PloS one*, vol. 14, e0222584, 2019.
[10] S. A. F. Council, "Fishery management plan for pelagic *Sargassum* habitat of the South Atlantic region," *Online) http://www. safmc. net/Portals/6/Library/FMP/Sargassum/SargFMP. pdf*, pp. 228, 2002.
[11] J. R. Rooker, J. P. Turner, and S. A. Holt, "Trophic ecology of *Sargassum*-associated fishes in the Gulf of Mexico determined from stable isotopes and fatty acids," *Marine Ecology Progress Series*, vol. 313, pp. 249-259, 2006.
[12] B. Witherington, S. Hirama, and R. Hardy, "Young sea turtles of the pelagic *Sargassum*-dominated drift community: habitat use, population density, and threats," *Marine Ecology Progress Series*, vol. 463, pp. 1-22, 2012.
[13] J. Partlow and G. Martinez, "Mexico deploys its navy to face its latest threat: Monster seaweed," *Washington Post, Oct*, vol. 28, p. 2015, 2015.
[14] A. Siuda, J. Schell, and D. Goodwin, "Unprecedented proliferation of novel pelagic *Sargassum* form has implications for ecosystem function and regional diversity in the Caribbean," in *AGU Fall Meeting Abstracts*, 2016.
[15] C. Hu, B. Murch, B. Barnes, M. Wang, J. Maréchal, J. Franks, *et al.*, "*Sargassum* watch warns of incoming seaweed," *EOS Trans. Am. Geophys. Union*, vol. 97, pp. 10-15, 2016.
[16] J. Rawlins-Bentham, "*Sargassum*: A national emergency and energy source. Barbados Government Information Service," ed, 2018.
[17] K. Langin, "Seaweed masses assault Caribbean islands," ed: American Association for the Advancement of Science, 2018.
[18] E. Doyle and J. Franks, "*Sargassum* fact sheet," 2015.
[19] R. Rodríguez-Martínez, A. Medina-Valmaseda, P. Blanchon, L. Monroy-Velázquez, A. Almazán-Becerril, B. Delgado-Pech, *et al.*, "Faunal mortality associated with massive beaching and decomposition of pelagic *Sargassum*," *Marine pollution bulletin*, vol. 146, pp. 201-205, 2019.
[20] B. I. van Tussenbroek, H. A. H. Arana, R. E. Rodríguez-Martínez, J. Espinoza-Avalos, H. M. Canizales-Flores, C. E. González-Godoy, *et al.*, "Severe impacts of brown tides caused by *Sargassum* spp. on near-shore Caribbean seagrass communities," *Marine Pollution Bulletin*, vol. 122, pp. 272-281, 2017.
[21] S. Djakouré, M. Araujo, A. Hounsou-Gbo, C. Noriega, and B. Bourlès, "On the potential causes of the recent Pelagic *Sargassum* blooms events in the tropical North Atlantic Ocean," *Biogeosciences Discuss.*, vol. 2017, pp. 1-20, 2017.
[22] C. A. Oviatt, K. Huizenga, C. S. Rogers, and W. J. Miller, "What nutrient sources support anomalous growth and the recent *sargassum* mass stranding on Caribbean beaches? A review," *Marine pollution bulletin*, vol. 145, pp. 517-525, 2019.
[23] J. S. Franks, D. R. Johnson, and D. S. Ko, "Pelagic *Sargassum* in the tropical North Atlantic," *Gulf and Caribbean Research*, vol. 27, pp. SC6-SC11, 2016.
[24] E. M. Johns, R. Lumpkin, N. F. Putman, R. H. Smith, F. E. Muller-Karger, D. Rueda, *et al.*, "The establishment of a pelagic *Sargassum* population in the tropical Atlantic: biological consequences of a basin-scale long distance dispersal event," *Progress in Oceanography*, p. 102269, 2020.
[25] J. Gower, S. King, G. Borstad, and L. Brown, "Detection of intense plankton blooms using the 709 nm band of the MERIS imaging spectrometer," *International Journal of Remote Sensing*, vol. 26, pp. 2005-2012, 2005.
[26] C. Hu, "A novel ocean color index to detect floating algae in the global oceans," *Remote Sensing of Environment*, vol. 113, pp. 2118-2129, 2009.
[27] L. Feng, C. Hu, B. B. Barnes, A. Mannino, A. K. Heidinger, K. Strabala, *et al.*, "Cloud and Sun-glint statistics derived from GOES and MODIS observations over the Intra-Americas Sea for GEO-CAPE mission planning," *Journal of Geophysical Research: Atmospheres*, vol. 122, pp. 1725-1745, 2017.

[28] R. F. Hardy, C. Hu, B. Witherington, B. Lapointe, A. Meylan, E. Peebles, *et al.*, "Characterizing a Sea Turtle Developmental Habitat Using Landsat Observations of Surface-Pelagic Drift Communities in the Eastern Gulf of Mexico," *IEEE Journal of Selected Topics in Applied Earth Observations and Remote Sensing*, vol. 11, pp. 3646-3659, 2018.

[29] R. K. Webster and T. Linton, "Development and implementation of *Sargassum* Early Advisory System (SEAS)," *Shore & Beach*, vol. 81, p. 1, 2013.

[30] D. Hedley, C. Roelfsema, V. Brando, C. Giardino, T. Kutser, S. Phinn. S, *et al.*," Coral reef applications of Sentinel-2: Coverage, characteristics, bathymetry and benthic mapping with comparison to Landsat 8," *Remote sensing of environment*, vol. 216, pp. 598-614, 2018.

[31] L. Biermann, D. Clewley, V. Martinez-Vicente, & K. Topouzelis, "Finding plastic patches in coastal Waters using optical Satellite Data," *Scientific reports*, vol. 10(1), pp. 1-10, 2020.

[32] L. Qi, C. Hu, K. Mikelsons, M. Wang, V. Lance, S. Sun, *et al*., "In search of floating algae and other organisms in global oceans and lakes," *Remote Sensing of Environment*, vol. 239, pp. 111659, 2020.

[33] R. A. Garcia, P. Fearns, J. K. Keesing, and D. Liu, "Quantification of floating macroalgae blooms using the scaled algae index," *Journal of Geophysical Research: Oceans*, vol. 118, pp. 26-42, 2013.

[34] L. Qi, C. Hu, Q. Xing, and S. Shang, "Long-term trend of *Ulva prolifera* blooms in the western Yellow Sea," *Harmful Algae*, vol. 58, pp. 35-44, 2016.

[35] L. Hu, K. Zeng, C. Hu, and M.-X. He, "On the remote estimation of *Ulva prolifera* areal coverage and biomass," *Remote sensing of environment*, vol. 223, pp. 194-207, 2019.

[36] F. Gascon, C. Bouzinac, O. Thépaut, M. Jung, B. Francesconi, J. Louis, *et al.*, "Copernicus Sentinel-2A calibration and products validation status," *Remote Sensing*, vol. 9, p. 584, 2017.

[37] Y. Chen and T. Pock, "Trainable nonlinear reaction diffusion: A flexible framework for fast and effective image restoration," *IEEE transactions on pattern analysis and machine intelligence*, vol. 39, pp. 1256-1272, 2016.

[38] Q. Vanhellemont and K. Ruddick, "Acolite for Sentinel-2: Aquatic applications of MSI imagery," in *Proceedings of the 2016 ESA Living Planet Symposium, Prague, Czech Republic*, 2016, pp. 9-13.

[39] M. A. Warren, S. G. Simis, V. Martinez-Vicente, K. Poser, M. Bresciani, K. Alikas, *et al.*, "Assessment of atmospheric correction algorithms for the Sentinel-2A MultiSpectral Imager over coastal and inland waters," *Remote sensing of environment*, vol. 225, pp. 267-289, 2019.

[40] S. Qiu, B. He, Z. Zhu, Z. Liao, and X. Quan, "Improving Fmask cloud and cloud shadow detection in mountainous area for Landsats 4–8 images," *Remote Sensing of Environment*, vol. 199, pp. 107-119, 2017.

[41] S. Foga, P. L. Scaramuzza, S. Guo, Z. Zhu, R. D. Dilley Jr, T. Beckmann, *et al.*, "Cloud detection algorithm comparison and validation for operational Landsat data products," *Remote sensing of environment*, vol. 194, pp. 379-390, 2017.

[42] D. Frantz, E. Haß, A. Uhl, J. Stoffels, and J. Hill, "Improvement of the Fmask algorithm for Sentinel-2 images: Separating clouds from bright surfaces based on parallax effects," *Remote sensing of environment*, vol. 215, pp. 471-481, 2018.

[43] M. Wang and W. Shi, "Cloud masking for ocean color data processing in the coastal regions," *IEEE Transactions on Geoscience and Remote Sensing*, vol. 44, pp. 3196-3105, 2006.

[44] A. Chambolle, "An algorithm for total variation minimization and applications," *Journal of Mathematical imaging and vision*, vol. 20, pp. 89-97, 2004.

[45] N. Pahlevan, S. Sarkar, B. Franz, S. Balasubramanian, and J. He, "Sentinel-2 MultiSpectral Instrument (MSI) data processing for aquatic science applications: Demonstrations and validations," *Remote sensing of environment*, vol. 201, pp. 47-56, 2017.

[46] D. C. Liu and J. Nocedal, "On the limited memory BFGS method for large scale optimization," *Mathematical programming*, vol. 45, pp. 503-528, 1989.

[47] Y. Chen, W. Yu, and T. Pock, "On learning optimized reaction diffusion processes for effective image restoration," in *Proceedings of the IEEE conference on computer vision and pattern recognition*, 2015, pp. 5261-5269.

[48] K. Dabov, A. Foi, V. Katkovnik, and K. Egiazarian, "Image denoising by sparse 3-D transform-domain collaborative filtering," *IEEE Transactions on image processing*, vol. 16, pp. 2080-2095, 2007.

[49] Z. Wang, A. C. Bovik, H. R. Sheikh, and E. P. Simoncelli, "Image quality assessment: from error visibility to structural similarity," *IEEE transactions on image processing*, vol. 13, pp. 600-612, 2004.

[50] T. P. Robitaille, E. J. Tollerud, P. Greenfield, M. Droettboom, E. Bray, T. Aldcroft, *et al.*, "Astropy: A community Python package for astronomy," *Astronomy & Astrophysics*, vol. 558, p. A33, 2013.

[51] A. Price-Whelan, B. Sipőcz, H. Günther, P. Lim, S. Crawford, S. Conseil, *et al.*, "The Astropy Project: Building an open-science project and status of the v2. 0 core package," *The Astronomical Journal*, vol. 156, p. 123, 2018.

[52] M. Wang and C. Hu, "Extracting oil slick features from VIIRS nighttime imagery using a Gaussian filter and morphological constraints," *IEEE Geoscience and Remote Sensing Letters*, vol. 12(10), pp. 2051-2055, 2015.

[53] N. Chinchor and B. Sundheim, "MUC-5 evaluation metrics," in *Proceedings of the 5th conference on Message understanding*, 1993, pp. 69-78.

[54] L. Feng and C. Hu, "Comparison of valid ocean observations between MODIS Terra and Aqua over the global oceans," *IEEE Transactions on Geoscience and Remote Sensing*, vol. 54, pp. 1575-1585, 2015.

[55] S. Sun, C. Hu, L. Feng, G. A. Swayze, J. Holmes, G. Graettinger, *et al.*, "Oil slick morphology derived from AVIRIS measurements of the Deepwater Horizon oil spill: Implications for spatial resolution requirements of remote sensors," *Marine pollution bulletin*, vol. 103, pp. 276-285, 2016.

[56] Z. Qiu, Z. Li, M. Bilal, S. Wang, D. Sun, and Y. Chen, "Automatic method to monitor floating macroalgae blooms based on multilayer perceptron: case study of Yellow Sea using GOCI images," *Optics express*, vol. 26, pp. 26810-26829, 2018.

[57] J. N. Butler, B. F. Morris, J. Cadwallader, and A. W. Stoner, "Studies of *Sargassum* and the *Sargassum* community," 1983, pp. 6-9.

[58] J. Arellano-Verdejo, H. E. Lazcano-Hernandez, and N. Cabanillas-Terán, "ERISNet: deep neural network for *Sargassum* detection along the coastline of the Mexican Caribbean," *PeerJ*, vol. 7, p. e6842, 2019.

[59] S. Wang, L. Liu, L. Qu, C. Yu, Y. Sun, F. Gao, *et al.*, "Accurate Ulva prolifera regions extraction of UAV images with superpixel and CNNs for ocean environment monitoring," *Neurocomputing*, vol. 348, pp. 158-168, 2019.